

ALICE-ANA-2017-xxx  
June 26, 2017

## $K^*(892)^\pm$ resonance production in pp collisions at $\sqrt{s} = 13$ TeV

Kunal Garg<sup>1,2</sup> and Angela Badalà<sup>2</sup>

1. University of Catania, Department of Physics and Astronomy, Catania, Italy

2. INFN, Sezione di Catania, Italy

Email: kgarg@cern.ch, angela.badala@ct.infn.it

### Abstract

Short lived resonances are good probes to study the properties of strongly interacting matter produced in high energy heavy ion collisions. In particular, the resonance  $K^*(892)^\pm$  is important because of its very short lifetime which is comparable to that of the fireball. The measurement of the  $K^*(892)^\pm$  meson reconstructed using its hadronic decay channel ( $K^*(892)^\pm \rightarrow \pi^\pm + K_S^0$ ) in minimum-bias pp collisions at  $\sqrt{s} = 13$  TeV is described in this note. The results, at mid-rapidity ( $|y| \leq 0.5$ ), include the transverse momentum ( $p_T$ ) spectra, the integrated yield  $dN/dy$ , the mean transverse momentum  $\langle p_T \rangle$ . Comparison of the inelastic  $p_T$  spectrum with prediction of PYHTIA6, PYTHIA8 and EPOS-LHC is also presented.  $K^*(892)^\pm$  results are compared to the  $K^*(892)^0$  results at the same collision energy.



## Contents

|          |   |           |
|----------|---|-----------|
| <b>1</b> | <b>Introduction</b>   | <b>2</b>  |
| <b>2</b> | <b>Data Set and event selection</b>                               | <b>2</b>  |
| 2.1      | Event selection . . . . .   | 2         |
| <b>3</b> | <b><math>\pi^\pm</math> and <math>K_S^0</math> selection</b>      | <b>3</b>  |
| 3.1      | Primary pion selection . . . . .                                  | 3         |
| 3.2      | $V^0$ selection . . . . .   | 4         |
| <b>4</b> | <b>Data analysis</b>  | <b>5</b>  |
| 4.1      | Signal extraction . . . . .                                       | 5         |
| 4.2      | Mass . . . . .  | 6         |
| 4.3      | Yield Extraction . . . . .  | 8         |
| <b>5</b> | <b>Monte Carlo correction estimates</b>                           | <b>10</b> |
| 5.1      | Acceptance $\times$ Efficiency . . . . .                          | 11        |
| 5.2      | Reweighted Acceptance $\times$ Efficiency . . . . .               | 11        |
| 5.3      | Signal-Loss correction . . . . .                                  | 13        |
| <b>6</b> | <b>Systematic uncertainties</b>                                   | <b>13</b> |
| 6.1      | Consistency Checks . . . . .                                      | 14        |
| 6.2      | Smoothing procedure for systematic uncertainties . . . . .        | 14        |
| 6.3      | Systematic due to signal extraction . . . . .                     | 14        |
| 6.4      | Systematic due to PID selection of primary tracks . . . . .       | 17        |
| 6.5      | Systematic due to secondary tracks selection + PID cuts . . . . . | 18        |
| 6.6      | Systematic due to topological cuts for $V^0$ selection . . . . .  | 20        |
| 6.7      | Systematic due to primary track selection . . . . .               | 21        |
| 6.7.1    | Primary track cuts . . . . .                                      | 21        |
| 6.7.2    | Global tracking . . . . .   | 22        |
| 6.8      | Systematic due to primary vertex selection . . . . .              | 22        |
| 6.9      | Systematic due to material budget . . . . .                       | 23        |
| 6.10     | Systematic due to hadronic interactions . . . . .                 | 23        |
| 6.11     | Total systematic uncertainty . . . . .                            | 23        |
| <b>7</b> | <b>Results</b>  | <b>29</b> |

|     |   |    |
|-----|---|----|
| 7.1 | Corrected $p_T$ spectrum . . . . .                    | 29 |
| 7.2 | Comparison with $K^*(892)^0$ $p_T$ spectrum . . . . . | 29 |
| 7.3 | $dN/dy$ and mean $p_T$ . . . . .                      | 30 |
| 7.4 | Comparisons to models . . . . .                       | 31 |

## 8 Appendix 32

Relevant Presentations:

**Resonances PAG Meeting, 27 July 2016:** [https://indico.cern.ch/event/559683/contributions/2258306/attachments/1316698/1973146/PAG\\_27th\\_July\\_2016.pdf](https://indico.cern.ch/event/559683/contributions/2258306/attachments/1316698/1973146/PAG_27th_July_2016.pdf)

**Resonances PAG Meeting, 07 December 2016:** <https://indico.cern.ch/event/593782/contributions/2399245/attachments/1384603/2106368/corr.pdf>

**Resonances PAG Meeting, 01 February 2017:** [https://indico.cern.ch/event/610692/contributions/2462365/attachments/1405373/2147565/PAG\\_1Feb2017.pdf](https://indico.cern.ch/event/610692/contributions/2462365/attachments/1405373/2147565/PAG_1Feb2017.pdf)

**Resonances PAG Meeting, 12 April 2017:** [https://indico.cern.ch/event/631075/contributions/2555773/attachments/1444252/2224670/PAG\\_12\\_Apr\\_2017\\_K\\_charged.pdf](https://indico.cern.ch/event/631075/contributions/2555773/attachments/1444252/2224670/PAG_12_Apr_2017_K_charged.pdf)

**Resonances PAG Meeting, 09 May 2017:** <https://indico.cern.ch/event/637781/contributions/2586970/attachments/1456523/2247903/PAG10May2017.pdf>

**Resonances PAG Meeting, 17 May 2017:** <https://indico.cern.ch/event/640004/contributions/2597343/attachments/1461545/2257768/PAG17May2017.pdf>

**Resonances PAG Meeting, 24 May 2017:** <https://indico.cern.ch/event/642012/contributions/2605488/attachments/1465476/2265334/PAG24May2017.pdf>

**Resonances PAG Meeting, 07 June 2017:** [https://indico.cern.ch/event/644567/contributions/2619793/attachments/1472218/2278644/PAG\\_7June\\_Kcharged.pdf](https://indico.cern.ch/event/644567/contributions/2619793/attachments/1472218/2278644/PAG_7June_Kcharged.pdf)

## 1 Introduction

$K^*(892)^\pm$  is a resonance particle with a small lifetime ( $\sim 4$  fm/c), comparable to that of the fireball which is produced during the heavy ion collision. Due to its short lifetime, it can be used to study the re-scattering and regeneration effects.  $K^*(892)^\pm$  can provide the information regarding strangeness enhancement as it contains a strange quark. Measurements of  $K^*(892)^\pm$  in pp collisions can be used as a baseline to study the Pb–Pb collisions at the LHC energy and to provide a reference for tuning event generators. This note describes the measurement of  $K^*(892)^\pm$  mesons (in the following  $K^{*\pm}$ ) produced at mid-rapidity ( $|y| \leq 0.5$ ) in minimum-bias pp collisions at  $\sqrt{s} = 13$  TeV. In this analysis,  $K^{*\pm}$  has been reconstructed by its hadronic decay channel  $K^*(892)^\pm \rightarrow \pi^\pm + K_S^0$ . The yield of  $K^{*\pm}$  is extracted from  $\pi K_S^0$  invariant-mass distributions as a function of transverse momentum. The  $p_T$  spectrum is integrated to obtain a measurement of the total  $dN/dy$ , and the mean transverse momentum  $\langle p_T \rangle$  is extracted from the spectrum.

## 2 Data Set and event selection

This analysis has been done using the data of pp collisions at centre of mass energy  $\sqrt{s} = 13$  TeV collected during 2015 (Run II). In particular, the Event Summary Data (ESD) pass2 of the period LHC15f (LHC15f/pass2/ESDs) were analyzed.

The following 48 runs were used:

225026, 225031, 225035, 225037, 225041, 225043, 225050, 225051, 225052, 225106, 225305, 225307, 225309, 225313, 225314, 225322, 225576, 225578, 225579, 225586, 225587, 225707, 225708, 225709, 225710, 225716, 225717, 225719, 225753, 225757, 225762, 225763, 225766, 225768, 226062, 226170, 226220, 226225, 226444, 226445, 226452, 226466, 226468, 226472, 226476, 226483, 226495, 226500.

For run number 225310, 225315, and 225705 TOF was not calibrated, but they can be used in this analysis that use only TPC information for PID. However for the moment we have used the same runs as  $K^*(892)^0$  analysis at the same energy [1].

For Monte Carlo we used the same runs of the production LHC15g3a3 for Monash 2013.

**AliPhysics version:** AliPhysics: VAN-20170511-1

### 2.1 Event selection

The analysis has been done for events with a z-vertex within  $\pm 10$  cm. The events were selected with a kINT7 trigger. The total number of events selected for this analysis is 46,18 million.

The following event-selection cuts were used:

- kINT7 trigger: This trigger should correspond to a logical AND between trigger inputs from V0A and V0C detectors.
- Standard Physics Selection.
- AliESDEvent::IsInCompleteDAQ check is used to reject events for which the event building does not work
- Pile-up events have been rejected using AliAnalysisUtils::IsPileUpEvent().
- SPD clusters vs. tracklets check using AliAnalysisUtils::IsSPDClusterVsTrackletBG() with default parameters.

- By default the track vertex is chosen. If it is missing, the vertex from the SPD is selected or at least event needs to have a track. Only events with vertex-z position  $|v_z| < 10$  cm have been taken into account.
- SPD vertex-z resolution  $< 0.25$  cm and SPD vertex dispersion  $< 0.04$  cm.
- z-position difference between track and SPD vertex  $< 0.5$  cm.

The z-distribution of the vertex of all accepted events is shown in the left panel of Fig. 1. In the right panel of Fig. 1 the same distribution in the Monte Carlo LHC15g3a3 production is shown. The two distributions are quite similar. Their difference will be tested in the systematic study.

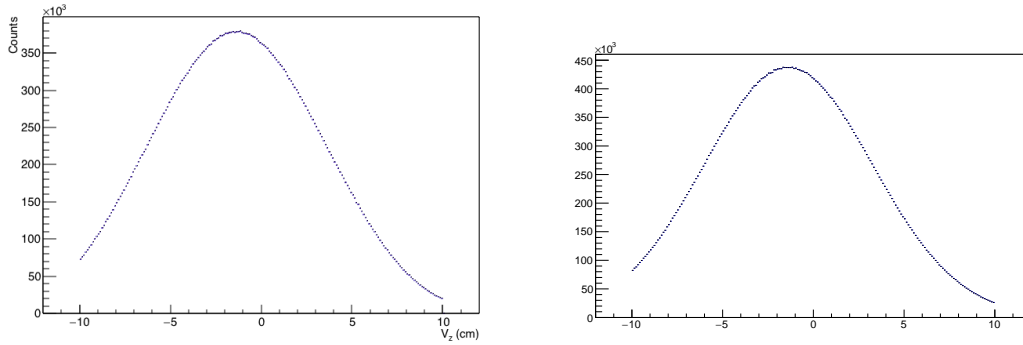


Fig. 1: (Left panel) The z-distribution of the vertex of all accepted events. (Right panel) The z-distribution of the vertex of all accepted events in the Monte Carlo LHC15g3a3 production.

### 3 $\pi^\pm$ and $K_S^0$ selection

The  $K^*(892)^\pm$  mesons were identified by reconstructing their decay in a charged pion ( $\pi^\pm$ ) and a  $K_S^0$ . Once identified a rapidity cut ( $|y| < 0.5$ ) has been applied to the pairs  $\pi^\pm V^0$ .

#### 3.1 Primary pion selection

Primary charged tracks were selected by applying the following cuts:

- $p_T > 0.15$  GeV/c
- $-0.8 < \eta < 0.8$
- Reject kink daughters
- Minimum number of rows crossed in TPC is 70
- Ratio of number of crossed rows to number of findable clusters in TPC  $> 0.8$
- Require TPC refit
- Require ITS refit
- TPC  $\chi^2$  per clusters  $< 4.0$
- ITS  $\chi^2$  per clusters  $< 36.0$
- $\chi^2$  per clusters in TPC-Constrained global fit  $< 36.0$
- Minimum number of clusters in SPD: 1 (AliESDtrackCuts::SetClusterRequirementITS(kSPD, kAny))

- AliESDtrackCuts::SetDCAToVertex2D(kFALSE)
- AliESDtrackCuts::SetRequireSigmaToVertex(kFALSE)
- $|DCA_z| < 2 \text{ cm}$
- $DCA_T < 0.0105 + 0.0350 p_T^{-1.1}$  (a  $7\sigma$   $p_T$  dependent cut)

These cuts, but the first two, are included in the function

**AliESDtrackCuts::GetStandardITSTPCTrackCuts2011(kTRUE, 1)** which implements the standard ITS/TPC track cuts from 2011.

The primary pions were identified through their energy loss  $dE/dx$  in the Time Projection Chamber (TPC). For this analysis due to problem with TPC PID wider TPC cuts were used at low momentum. The following  $p$ -dependent PID selection cuts were applied:

- $|N\sigma_{\text{TPC}}| < 6$  for  $p < 0.3 \text{ GeV}/c$
- $|N\sigma_{\text{TPC}}| < 4$  for  $0.3 \leq p \leq 0.4 \text{ GeV}/c$
- $|N\sigma_{\text{TPC}}| < 3$  for  $p > 0.4 \text{ GeV}/c$

In Fig. 2  $N\sigma_{\text{TPC}}$  versus momentum  $p$  for pions without any PID cut (left panel) and after that  $p$ -dependent PID cut is applied (right panel) are shown.

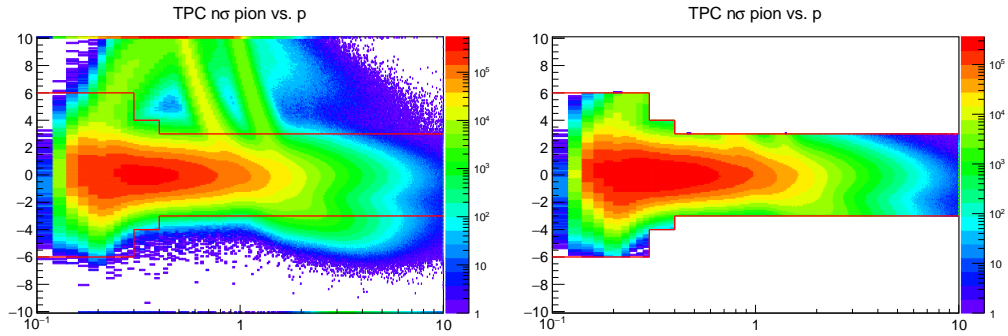


Fig. 2:  $N\sigma_{\text{TPC}}$  versus momentum  $p$  for pions without any PID cut (left panel) and after  $p$ -dependent PID cut is applied (right panel). The dotted lines indicate the TPC PID cuts as a function of momentum.

### 3.2 $V^0$ selection

The  $V^0$   $K_S^0$  is identified by its decay  $K_S^0 \rightarrow \pi^+ + \pi^-$ .

The following selection criteria were applied to select the secondary pions.

#### Daughter track selection criteria

- $-0.8 < \eta < 0.8$
- Require TPC refit
- Reject Kink Daughters
- Minimum number of rows crossed in TPC  $> 70$
- Ratio of number of crossed rows to number of findable clusters in TPC  $> 0.8$

- TPC  $\chi^2/\text{clusters} < 4.0$
- DCA of tracks to PV  $> 0.0105 + 0.0350 p_T^{-1.1}$  cm (a  $p_T$  dependent cut to be complementary to primary tracks)

Furthermore secondary pions were identified through their energy loss  $dE/dx$  in the Time Projection Chamber (TPC), by a wide PID cut  $|N\sigma_{\text{TPC}}| < 5$ .

The pairs of  $\pi^+\pi^-$  which fulfill the following  **$V^0$  selection criteria** were taken as  $K_S^0$  candidates

- Only Offline  $V^0$
- Rapidity  $|y| < 2.0$
- Fiducial Volume ( $V^0$  2D decay radius)  $> 0.5$  cm
- $V^0$  cosine of pointing angle  $> 0.97$
- DCA  $V^0$  to Primary Vertex  $< 0.3$  cm
- DCA  $V^0$  daughters  $< 1.0 \sigma$
- $V^0$  Mass Tolerance  $< 0.03 \text{ GeV}/c^2$
- Proper Lifetime ( $mL/p$ )  $< 20$  cm

The previous cuts are the same used for the identification of  $K_S^0$  in pp collisions at  $\sqrt{s} = 13 \text{ TeV}$  [2]. Only difference is for the  $V^0$  mass cut. A  $V^0$  mass tolerance cut was added to well select  $K_S^0$  particles. On the contrary, the competing  $V^0$  rejection was not used since a slightly decrease of the signal without any increasing of its significance was observed. In case this rejection is used only pairs that have an invariant mass incompatible with the hypothesis to be originated from a  $\Lambda$  or  $\bar{\Lambda}$  decay ( $|M_\Lambda - 1115.683| > 4 \text{ MeV}/c^2$  or  $|M_{\bar{\Lambda}} - 1115.683| > 4 \text{ MeV}/c^2$ ) would be taken. Furthermore considering that we are interested only to "primary"  $V^0$  a cut of 0.3 cm was applied on the DCA of the  $V^0$  to the primary vertex.

## 4 Data analysis

### 4.1 Signal extraction

The raw yield of  $K^*(892)^\pm$  was estimated in the following 19  $p_T$  bins (0, 0.3, 0.7, 1.2, 1.4, 1.6, 1.8, 2.0, 2.4, 2.8, 3.2, 3.6, 4.0, 5.0, 6.0, 7.0, 8.0, 10.0, 12.0, 15.0). To extract the signal of  $K^*(892)^\pm$  mesons in each  $p_T$  bin, the following procedure were used. First the invariant-mass distribution of  $K_S^0\pi^\pm$  pairs were computed in the same event. This gave a peak over a large combinatorial background, which was estimated by the event-mixing technique. In this method, the shape of the uncorrelated background is estimated from the invariant mass distribution of pions and  $K_S^0$  pairs from different events. To avoid mismatch due to different acceptance and to assure a similar event structure, particles from events with similar vertex position  $z$  ( $\Delta z < 1$  cm and track multiplicity  $n$  ( $\Delta n < 5$ )) were used. To reduce statistical uncertainties each event was mixed with other 10 events. The mixed-event distribution was then normalized to the same event distribution in the invariant mass region of  $1.1 < M < 1.2 \text{ GeV}/c^2$ . The signal is obtained by subtracting the mixed-event combinatorial background from the same event invariant mass distribution. The  $K_S^0\pi^\pm$  invariant mass distribution for the bin  $1.6 < p_T < 1.8 \text{ GeV}/c$  with the background estimated by pairs of different events are shown in the left panel of Fig. 3. For the same  $p_T$  bin the signal obtained after background subtraction is shown in the right panel of the same figure. Same distributions for all the  $p_T$  bins are reported in Fig. 32 and Fig. 33.



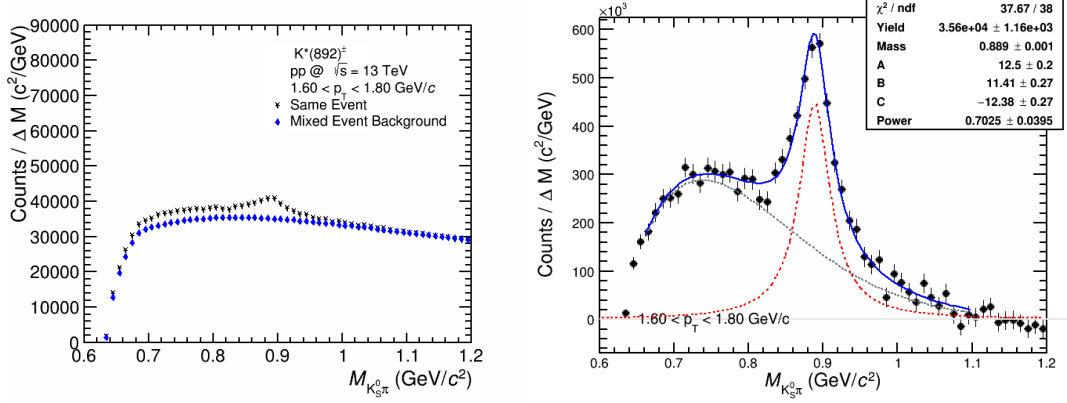


Fig. 3: (Left panel) The  $K_S^0 \pi^\pm$  invariant mass distribution in  $|y| < 0.5$  for the bin  $1.6 < p_T < 1.8$  GeV/c in pp collisions at  $\sqrt{s} = 13$  TeV. The background shape estimated using pairs from different events (event-mixing technique) is shown as open green circles. (Right panel) The  $K_S^0 \pi^\pm$  invariant mass distribution for the bin  $1.6 < p_T < 1.8$  GeV/c after background subtraction. The solid red curve is the results of the fit by eq. 4, the dashed blue (green) curve describes the residual background (Breit-Wigner distribution).

## 4.2 Mass

The PDG [3] mass and width of the  $K^*(892)^\pm$  are  $891.66 \pm 0.26$  MeV/ $c^2$  and  $50.8 \pm 0.9$  MeV/ $c^2$ , respectively. To estimate the mass and the width of the resonance the background-subtracted invariant mass distribution was fitted by a function given by the sum of a function to describe the shape of the resonance and a second order polynomial to take into account the residual background. The shape of the resonance is described with a relativistic Breit-Wigner function with a dependent mass width multiplied by a Boltzmann factor to take into account the effect of the available phase space. The fitting function is:

$$\frac{AM_{K\pi}M_0\Gamma_{M_{K\pi}}}{(M_0^2 - M_{K\pi}^2) + M_0\Gamma_{M_{K\pi}}^2} \times PS(M_{K\pi}) + Polynomial \quad (1)$$

where  $M_0$  is the mass of the  $K^*(892)^\pm$ . To take into account the dependence of the resonance width on the mass the following function is used for  $\Gamma_{M_{K\pi}}$ .

$$\Gamma_{M_{K\pi}} = \left( \frac{M_{K\pi}^2 - (m_\pi + m_K)^2}{M_0^2 - (m_\pi + m_K)^2} \right)^{(2J+1)/2} \times \Gamma_0 \times M_0/M_{K\pi} \quad (2)$$

where  $\Gamma_0$  is the width of the  $K^*(892)^\pm$ ,  $m_\pi$  and  $m_K$  are respectively the mass of the charged pion and of the  $K_S^0$ . The spin  $J$  is equal to 1 in our case.

The phase-space factor was taken into account by a Boltzmann factor:

$$PS(M_{K\pi}) = \frac{M_{K\pi}}{\sqrt{M_{K\pi}^2 + p_T^2}} \times \exp(-\sqrt{M_{K\pi}^2 + p_T^2}/T) \quad (3)$$

where  $T$  is the kinetic freeze-out temperature set to 160 MeV in pp collisions [4]. A first fit was done with all the parameters free, in particular mass and width. Mass values for the different  $p_T$  bins are reported in the left panel of Fig. 4. The width extracted for the different  $p_T$  bins, when the signal is fitted by a relativistic Breit-Wigner (i.e. without considering the PS correction), is shown in the right panel of Fig. 4. It is worth to note as the width is roughly equal to the PDG value [3]. In the left panel of Fig. 4 the mass obtained fitting the invariant mass distributions of the different  $p_T$  bins with the width parameter fixed to PDG value is shown. No large differences as observed for the mass when the width is fixed or free. A mass lower than the PDG value is obtained, especially for  $p_T < 2.5$  GeV/c. It is interesting to

note as a similar behaviour is present in Monte Carlo data. In this case the shape of the resonance was parameterized only with a relativistic Breit-Wigner function.

In Fig. 6 the  $K^*(892)^\pm$  reconstruction efficiencies (rescaled to the value at  $M = 0.892 \text{ GeV}/c^2$ ) versus mass at various  $p_T$  bins are shown. The same definition of that used to estimate the standard efficiency (Eq. 10) was used. A dependence of the efficiency from the invariant mass is clearly seen. In particular, for  $p_T < 0.7 \text{ GeV}/c$  the efficiency increases with the mass, while it is constant for  $0.7 < p_T < 1.2 \text{ GeV}/c$  and then decreases with the mass at higher  $p_T$ . It returns constant for  $p_T > 3.5 \text{ GeV}/c$ . By a linear fit in the range  $0.76 < M_{K\pi} < 1.1 \text{ GeV}/c^2$  a correction function was estimated for all the  $p_T$  bins (colored lines in Fig. 6). The invariant mass distributions of the different  $p_T$  bins were corrected for the mass dependent efficiencies and fitted by a relativistic Breit-Wigner + a second order polynomial (with width fixed to PDG value). The comparison of the obtained  $M_0$  values compared to the one estimated with the same fitting function when no mass efficiency correction is applied is shown in Fig. 5. No substantial difference is observed between the two extracted mass values.

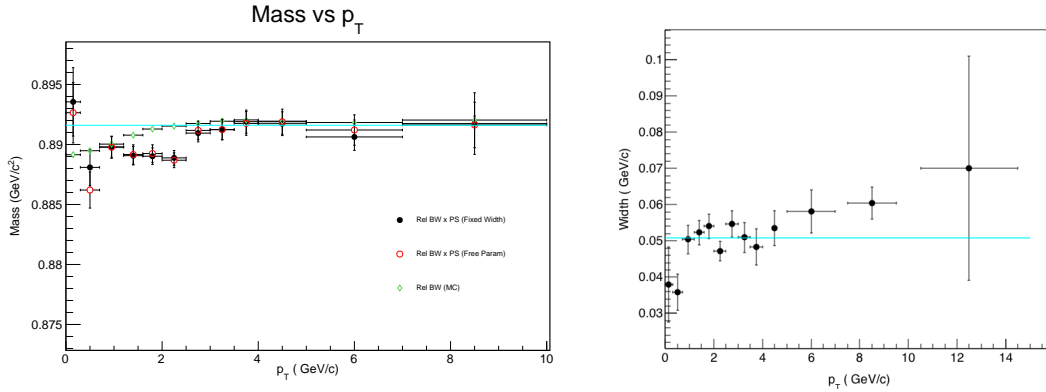


Fig. 4: (Left panel) Mass vs.  $p_T$  for data and Monte Carlo. Signal in Monte Carlo is fitted with a relativistic Breit-Wigner. For data signal is fitted with Eq.1, with the width free (empty red squares) and fixed (black squares) to the PDG value. (Right panel) Width vs.  $p_T$  obtained from data fitted with a relativistic Breit-Wigner function. The sky-blue line represents the PDG value for the width.

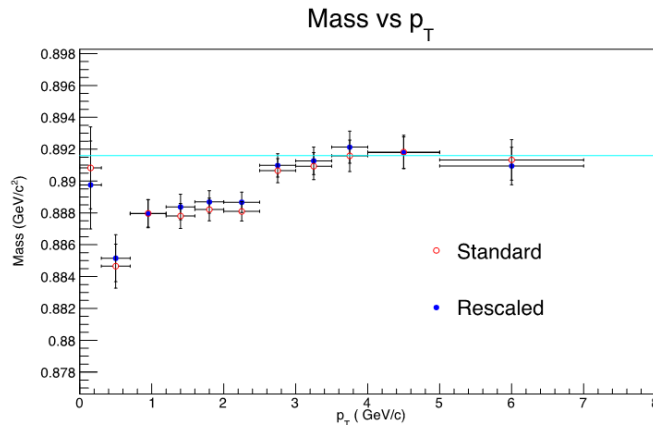


Fig. 5: Mass vs.  $p_T$  obtained fitting the standard (empty red circles) and mass-efficiency corrected (blue circles) invariant mass distribution by a relativistic Breit-Wigner + a second order polynomial (with width fixed to PDG value). The sky-blue line represents the PDG value for the mass.

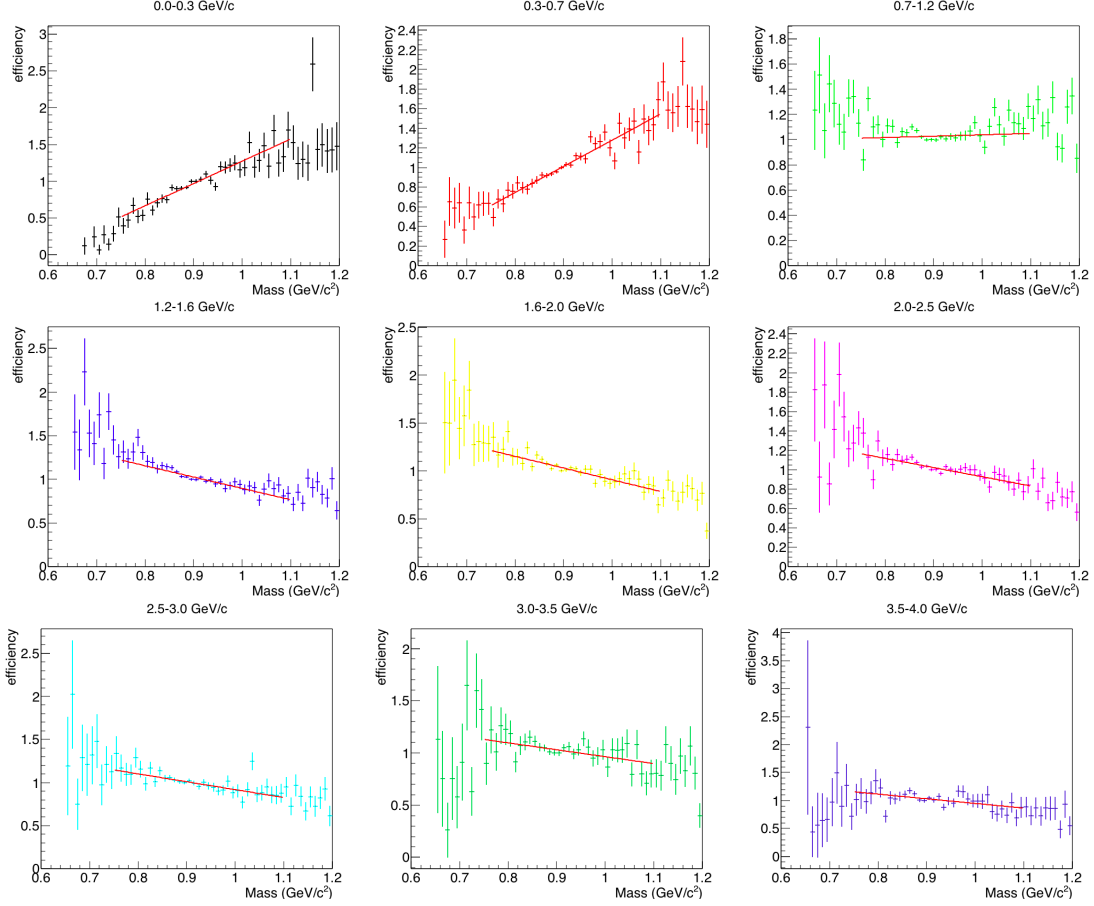


Fig. 6: Efficiency vs. invariant mass for different  $p_T$  bins. Efficiency is rescaled to the value at  $M = 0.892 \text{ GeV}/c^2$ . The colored lines represent the linear fit done in the range  $0.76 < M < 1.1 \text{ GeV}/c^2$ .

### 4.3 Yield Extraction

The invariant mass distribution obtained after the subtraction of the combinatorial background estimated by the event mixing was fitted with a non-relativistic Breit-Wigner + background function.

$$\frac{A}{2\pi} \frac{\Gamma_0}{(M_{K\pi} - M_0)^2 + \frac{\Gamma_0^2}{4}} + F_{BG} \quad (4)$$

where  $M_0$  and  $\Gamma_0$  are the mass and the width of the  $K^*(892)^\pm$ . The parameter  $A$  is the integral of the peak function from 0 to  $\infty$ .

The residual background shape for the different  $p_T$  bins was extracted from Monte Carlo simulated data. First, 2nd and 3rd order polynomial were tested as residual background function. However the best parameterisation of the background was given from the following function already used in [5]:

$$F_{BG}(M_{K\pi}) = [M_{K\pi} - (m_\pi + m_K)]^n \exp(A + BM_{K\pi} + CM_{K\pi}^2) \quad (5)$$

where  $m_\pi = 139.57018 \text{ GeV}/c^2$  [3] and  $m_K = 497.611 \text{ GeV}/c^2$  [3] are the pion and  $K_S^0$  mass and  $n$ ,  $A$ ,  $B$  and  $C$  are fit parameters.

To have a good fit the width was fixed to its PDG value. The fitting range was chosen accurately for each  $p_T$  bins to improve the global  $\chi^2$  of the fit. For the large part of the  $p_T$  bins the fit range was  $0.66 - 1.1 \text{ GeV}/c^2$ . The results of the fit for the different  $p_T$  bins are reported in Fig. 33. The solid red curve is the results of the fit, the dashed blue line describes the residual background while the dashed green curve is the non-relativistic Breit-Wigner which describes the  $K^*(892)^\pm$  peak.

The raw yield of  $K^*(892)^\pm$  was calculated using two different methods: the fit function ( $Y_{FI}$ ) or bin counting ( $Y_{BC}$ ), where the second was used as default and the first was used for systematic study.

**Function Integral( $Y_{FI}$ ):** The parameter  $A$  of the fit is the integral of the peak function from 0 to  $\infty$ , but the mass region  $0 < M_{K\pi} < (m_\pi + m_K)$ , where  $m_\pi = 139.57018 \text{ GeV}/c^2$  [3] and  $m_K = 497.611 \text{ GeV}/c^2$  [3] are respectively the mass of the charged pion and of the  $K_S^0$ , is kinematically forbidden. Therefore

$$Y_{FI} = A - \int_0^{m_\pi+m_K} fit(m_{inv}) dm_{inv} \quad (6)$$

The integral in the kinematically forbidden region is about 2.5 % of the total integral, with the exact ratio depending on the peak parameters.

### Bin counting ( $Y_{BC}$ ):

The raw yield ( $N_{BC}$ ) in the region  $I_{min} < M_{K\pi} < I_{max}$  (where  $I_{min} = M_0 - \Gamma_0$  ( $0.79 \text{ GeV}/c^2$ ) and  $I_{max} = M_0 + \Gamma_0$  ( $0.99 \text{ GeV}/c^2$ ), respectively) was extracted by integrating the invariant mass histogram ( $N_{counts}$ ) over the region  $I_{min} < M_{K\pi} < I_{max}$  and subtracting the integral of the residual background portion estimated over that same interval ( $N_{RB}$ ).

$$N_{BC} = N_{counts} - N_{RB} \quad (7)$$

The error on  $N_{RB}$  was calculated by using the the root function `fBgOnly`  $\rightarrow$  `IntegralError( $I_{min}$ ,  $I_{max}$ , Par[4], $a$ )`, where  $a$  is the covariance matrix, `fBgOnly` is the residual background function and `Par[4]` is a vector with the value of the parameters of the residual background function. To obtain the total raw yield we have to correct the  $N_{raw}$  value for the the yields in the regions  $m_\pi + m_K < M_{K\pi} < I_{min}$  ( $N_{low}$ ) and  $M_{K\pi} > I_{max}$  ( $N_{high}$ ).  $N_{low}$  and  $N_{high}$  were estimated integrating in the regions  $m_\pi + m_K < M_{K\pi} < I_{min}$  and  $I_{max} < M_{K\pi} < \infty$  the non-relativistic Breit-Wigner function extracted from the fit.

$$N_{low} = \int_{m_\pi+m_K}^{M_0-\Gamma_0} fit(m_{inv}) dm_{inv} \quad (8)$$

$$N_{high} = \int_{M_0+\Gamma_0}^{\infty} fit(m_{inv}) dm_{inv} \quad (9)$$

This accounts for about 13% of the total yield. The total raw yield was obtained adding low and high invariant mass tail contributions to the bin counting yield.

$$N_{raw} = N_{BC} + N_{low} + N_{high}$$

It is assumed that the statistical uncertainties of the yields in the tail regions are fully correlated with each other and with the statistical uncertainty of the yield calculated from the histogram.

In Fig. 7 the raw yield  $p_T$  distributions obtained with the two methods are compared. Variation in the measured  $K^*(892)^\pm$  meson yield between these methods were taken into account in the estimation of the systematic uncertainties (see Section 6).

Considering that for  $p_T > 3 \text{ GeV}/c$  the event mixing shape is not able to describe the background, we have tried to estimate the yield fitting the invariant mass distributions without any background subtraction with the 4 with background described by 5. The result obtained for the  $p_T$  bin 6 -7  $\text{GeV}/c$  is shown in left panel of Fig. 8. In the right panel of Fig. 8 it is reported as a function of  $p_T$  the ratio of the yields obtained by the standard fit procedure (i.e fitting the distribution after the background subtraction) and by fitting the invariant mass distribution without background subtraction. These differences were then used in the estimation of the systematic uncertainties.

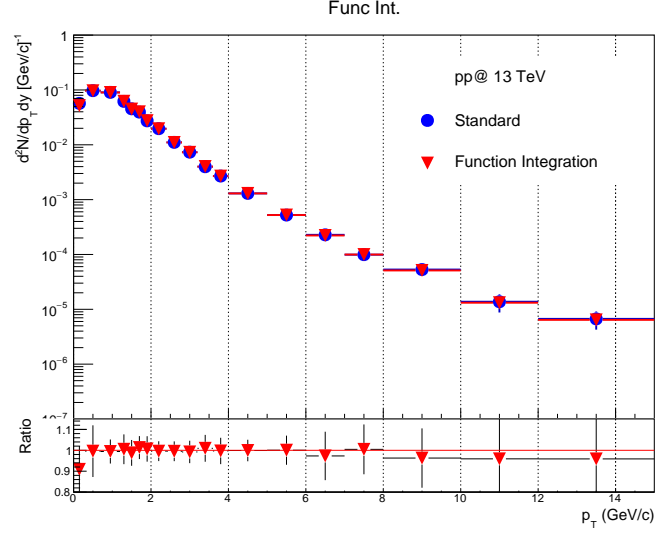


Fig. 7: Transverse momentum raw yield distributions estimated by bin-counting method (blue circles) and by function integration (red triangles). Ratio of the two distributions (bin-counting/function integration) is shown in the lower panel.

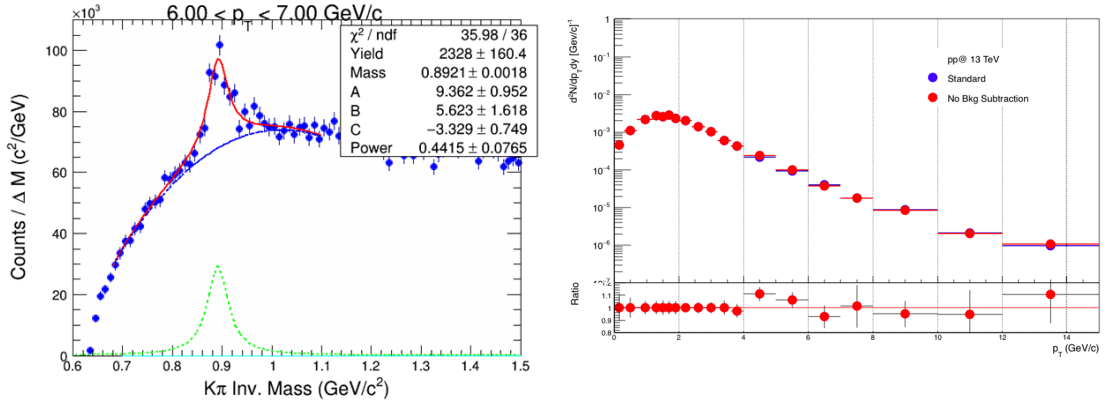


Fig. 8: (Left panel) The  $K_S^0 \pi^\pm$  invariant mass distribution in  $|y| < 0.5$  in pp collisions at 13 TeV for  $6 \leq p_T \leq 7$ . The solid red curve is the results of the fit by eq. 4, the dashed blue (green) line describes the residual background (non-relativistic Breit-Wigner) distribution. (Right panel) Ratio of the yields obtained by the standard fit procedure (i.e fitting the distribution after the background subtraction) and by fitting the invariant mass distribution without background subtraction.

## 5 Monte Carlo correction estimates

A simulated data set was analysed in order to extract the  $K^*(892)^\pm$  reconstruction efficiency  $\times$  acceptance. The following data sets (ESD) are available: LHC15g3a3 production (Monash 2013 tune of PYTHIA 8) with 51.5 million events, LHC15g3c3 production (Perugia 2011 tune of PYTHIA 6) with 49.0 million events and LHC16d3 production (EPOS-LHC) with 51.2 million events. Particle production and decays are simulated using the event generator while particle interactions with the ALICE detector are simulated using GEANT3. The same event selection, track quality cuts and topological cuts were used for the real and simulated data. The particles produced by the event generator (without any detector effects) are referred to as the "generated" particles. These particles are the input for the GEANT3 detector simulation and the track,  $V^0$  and signal reconstruction algorithms. The tracks and the  $V^0$  which are identified by the reconstruction algorithms and which pass track and topological selection and PID cuts are referred to

as "reconstructed" tracks and  $V^0$ . A reconstructed  $K^*(892)^\pm$  meson is a  $K^{*\pm}$  for which both daughters (track and  $V^0$ ) have been reconstructed.

### 5.1 Acceptance $\times$ Efficiency

The reconstruction acceptance $\times$ efficiency, denoted  $\epsilon_{rec}$ , was calculated using LHC15g3a3, LHC15g3c3 and LHC16d3 simulation sets. The average of the the 3  $\epsilon_{rec}$  was used. In the left panel of Fig. 9 the comparison of the acceptance $\times$ efficiency distributions obtained with the 3 Monte Carlo sets is shown.

In each transverse momentum bin,  $\epsilon_{rec}$  is given by

$$\epsilon_{rec} = \frac{N_{reconstructed}}{N_{generated}} \quad (10)$$

where  $N_{generated}$  is the number of generated  $K^*(892)^\pm$  mesons with  $|y| < 0.5$  that decay in a  $K_S^0$  and a charged pion ( $\pi^\pm$ );  $N_{reconstructed}$  is the number of reconstructed  $K^*(892)^\pm$  mesons with  $|y| < 0.5$ .

The  $K^*(892)^\pm$  efficiency $\times$ acceptance distribution as a function of  $p_T$  is shown in the right panel of Fig. 9. It has a strong dependence on transverse momentum at low  $p_T$ . In the same figure the  $K^*(892)^0$  acceptance $\times$ efficiency is also shown.

Since the events of numerator and denominator are correlated the uncertainty in  $\epsilon_{rec}$  was calculated using the Bayesian approach described in [6]. The standard deviation in an efficiency  $\epsilon = k/n$ , where the numerator  $k$  is a subset of the denominator  $n$ , is:

$$\sigma_\epsilon = \sqrt{\frac{k+1}{n+2} \left( \frac{k+2}{n+3} - \frac{k+1}{n+2} \right)} \quad (11)$$

The fractional statistical uncertainty in  $\epsilon_{rec}$  was added in quadrature with the statistical uncertainty in the uncorrected  $K^*(892)^\pm$  yield to give the total statistical uncertainty of the corrected  $K^*(892)^\pm$  yield.

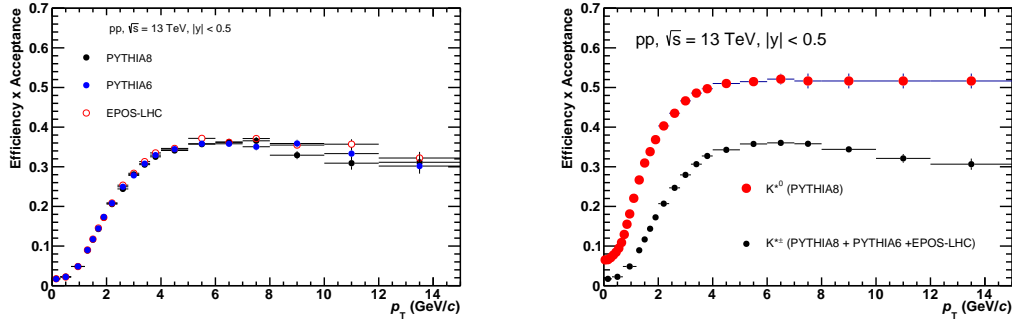


Fig. 9: (Left panel) Comparison of the acceptance $\times$ efficiency distributions obtained with LHC15g3a3 (PYTHIA8), LHC15g3c3 (PYTHIA6) and LHC16d3 (EPOS-LHC) productions. (Right panel) Acceptance $\times$ Efficiency of  $K^*(892)^\pm$  and  $K^*(892)^0$  mesons as a function of  $p_T$ .

### 5.2 Reweighted Acceptance $\times$ Efficiency

If the generated spectrum has a different shape than the measured resonance spectrum, it is necessary to weight the generated and reconstructed spectra. Figure 10 shows the generated  $K^*(892)^\pm$  spectra (average of the three  $p_T$  spectra) plotted with the (corrected) measured  $K^*(892)^\pm$  spectrum and the Levy-Tsallis fit (see Section 7.3) of that measured spectrum. The standard resonance macro for the reweighting ALICE PHYSICS/PWGLF/RESONANCES/macros/Utils/ReweightEfficiency.C was used. This macro starting from the corrected resonance spectrum and the generated and reconstructed spectra (used to estimate the  $\epsilon_{rec}$ ) determines the weighting to correct  $\epsilon_{rec}$  with the following iterative procedure.

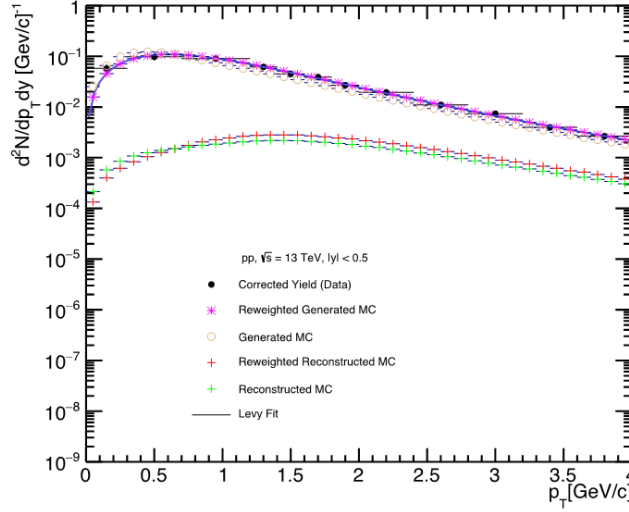


Fig. 10: Corrected  $K^*(892)^\pm$  spectrum (black dots) with Levy-Tsallis fit (black curve). The unweighted generated (brown circles) distribution is compared to the reweighted one (purple crosses). The reweighted reconstructed (red crosses) and the reconstructed (green crosses) spectra are also shown.

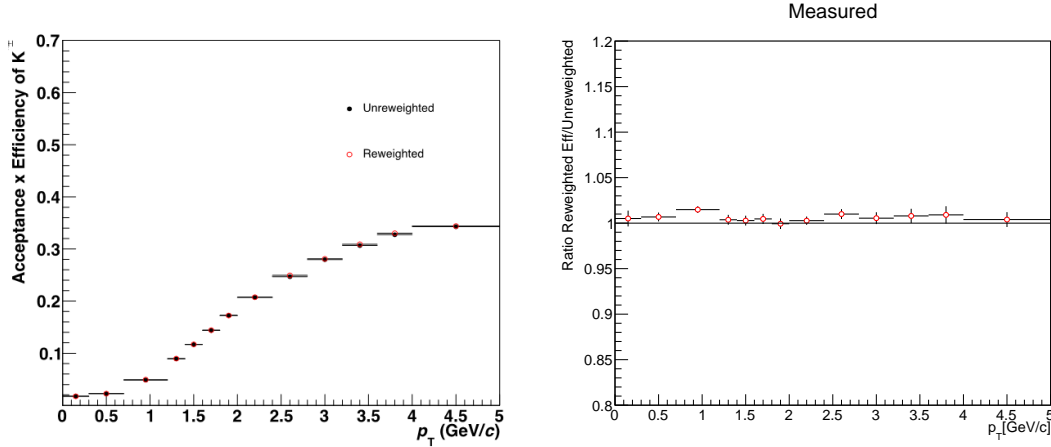


Fig. 11: (Left panel) Comparison of weighted and unweighted efficiency. (Right panel) Ratio of weighted and unweighted efficiency.

- 1) The unweighted  $\epsilon_{rec}$  is calculated using the generated and reconstructed  $K^{*\pm}$  spectra.
- 2) This  $\epsilon_{rec}$  is used to correct the measured  $K^{*\pm}$  spectrum.
- 3) The corrected  $K^*(892)^\pm$  spectrum is fitted using a Levy-Tsallis function.
- 4) This fit is used to weight the simulated  $K^{*\pm}$  spectra. A  $p_T$ -dependent weight is applied to the generated spectrum so that it follows the fit. The same weight is applied to the reconstructed spectrum.
- 5) The (weighted)  $\epsilon_{rec}$  is calculated (see Fig. 11).
- 6) Steps 2-5 are repeated (with the weighted  $\epsilon_{rec}$  from step 5 used as the input for step 2) until the  $\epsilon_{rec}$  values are observed to change by less than 0.1% between iterations. It was observed that two iterations are usually sufficient for this procedure to converge.

In the left panel of Fig. 11 the weighted and unweighted efficiency are compared. Their ratio is plotted in the right panel.

### 5.3 Signal-Loss correction

The signal-loss correction  $\varepsilon_{SL}$  accounts for the loss of  $K^*(892)^\pm$  mesons incurred by selecting events that satisfy the kINT7 trigger, rather than all inelastic events. This is a  $p_T$ -dependent correction factor which is peaked at low  $p_T$ , indicating that events that fail the kINT7 selection have softer  $K^{*\pm}$   $p_T$  spectra than the average inelastic event. This correction is the ratio of the  $p_T$  spectrum in inelastic events to the  $p_T$  spectrum in kINT7 events. The  $p_T$  spectrum in inelastic events were generated without any trigger selection and with a check that the generated vertex is inside  $\pm 10$  cm (SetCheckGeneratedVertexZ option was used). The  $\varepsilon_{SL}$  was estimated using two different productions: LHC15g3a3 (PYTHIA8) and LHC15g3c3 (PYTHIA6). The obtained  $p_T$  distributions of the signal-loss correction with the different Monte Carlo production are shown in Fig. 12. They are slightly different especially at low  $p_T$ . To be uniform with other resonance analyses at the same collision energy the  $\varepsilon_{SL}$  distribution obtained with PYTHIA8 was used to estimate the  $K^*(892)^\pm$  inelastic  $p_T$  spectrum. The uncertainty of this correction was estimated as the difference between PYTHIA8 and PYTHIA6 distribution.

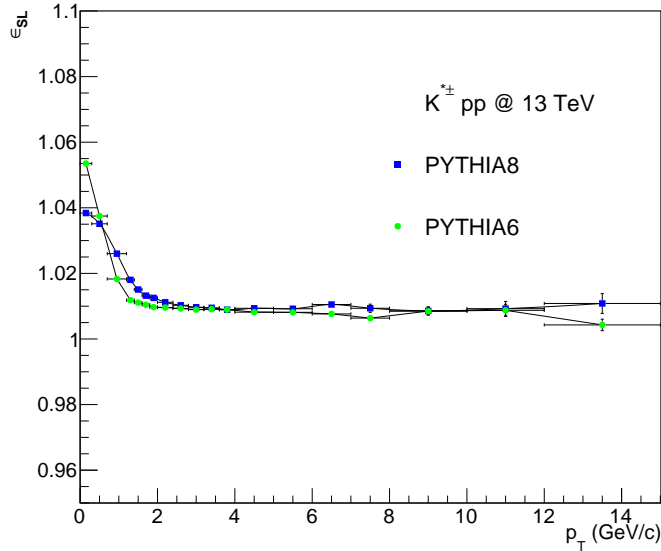


Fig. 12: Comparison of signal-loss correction ( $\varepsilon_{SL}$ )  $p_T$  distribution estimated with LHC15g3a3 (PYTHIA8) and LHC15g3c3 (PYTHIA6) production.

## 6 Systematic uncertainties

For the  $p_T$  spectrum the following sources of systematic uncertainty were considered: Signal extraction, primary track selection, PID cut for primary pions, secondary track selection + PID, topological cuts for  $K_S^0$ , event selection, material budget, hadronic interaction. The general strategy for evaluating systematic uncertainties for the  $p_T$  spectrum was:

- 1) Observe the deviations in the yield of each  $p_T$  bin when one of the "standard" parameters is changed. Two or more variations can be considered for each parameters.
- 2) If the observed variations for all the  $p_T$  bins were found to be not consistent (Barlow check, see 6.1), for each  $p_T$  bin the largest variation was taken as systematic uncertainty due to this parameter.



- 3) For each  $p_T$  bin the systematic uncertainties of different parameters were added in quadrature to obtain the total systematic uncertainty of a given source.
- 4) A smoothing procedure was applied if the systematic uncertainties exhibit a few large fluctuations from bin to bin
- 5) The systematic uncertainties from different sources were added in quadrature to obtain the total systematic uncertainty.

### 6.1 Consistency Checks

This analysis was run many times with many different analysis parameters varied. However, it is necessary to ensure that the systematic uncertainties are not simply accounting for statistical fluctuations. As described in [7], the condition for consistency is not agreement within the statistical uncertainties. Since the default and alternate measurements use (mostly) overlapping data sets, agreement within the statistical uncertainties is not sufficient. Instead, agreement within the difference in quadrature of the statistical uncertainties is required. If two measurements are found to be consistent within the quadrature difference of their statistical uncertainties, then it is not necessary to account for the differences between them in the systematic uncertainties. As an example, consider two  $p_T$  spectra, one obtained with the default setting and a second obtained with an alternative setting (for example, with a different normalization range). Let us denote the yield and the statistical uncertainty as  $y_{def}$  and  $\sigma_{def}$  for the default case and as  $y_{al}$  and  $\sigma_{al}$  for the alternative setting. For each  $p_T$  bin we can estimate  $\Delta/\sigma_{cc}$ , where  $\Delta$  is the difference between the default and the alternative measurement ( $\Delta = y_{def} - y_{al}$ ) and  $\sigma_{cc}$  is the difference in quadrature of the statistical uncertainties of these measurements ( $\sigma_{cc} = \sqrt{\sigma_{def}^2 - \sigma_{al}^2}$ ). In general, if two measurements are consistent, it is expected that the distribution of  $\Delta/\sigma_{cc}$  would have a mean near 0, a standard deviation near 1, and that 68% (95%) of the entries would lie within  $|\Delta/\sigma_{cc}| < 1$  ( $|\Delta/\sigma_{cc}| < 2$ ). For this analysis we don't consider a parameter as a systematic source if 3 of the following 4 criteria are satisfied:  $|\Delta/\sigma_{cc}| < 0.1$ , standard deviation  $< 1.1$ , fraction of entries within  $\pm 1$  ( $I_1 > 0.55$ ), fraction of entries within  $\pm 2$  ( $I_2 > 0.85$ ).

### 6.2 Smoothing procedure for systematic uncertainties

The systematic uncertainties exhibit a few large fluctuations from bin to bin, while one might expect the "true" systematic uncertainties to be more uniform or smoothly varying. The total systematic uncertainty was not directly smoothed; rather, each source of systematic uncertainty was smoothed individually. If necessary, the following smoothing procedure was applied. For  $p_T$  bin  $j$  the uncertainty  $\sigma_j^{i+1}$  was obtained averaging the initial uncertainty  $\sigma_j^i$  with  $\sigma_{j\pm 1}^i$ , i.e.

$$\sigma_j^{i+1} = (\sigma_{j-1}^i + \sigma_j^i + \sigma_{j+1}^i)/3 \quad (12)$$

If necessary the smoothing procedure was iterated. First and last bin remain unchanged during the smoothing procedure.

### 6.3 Systematic due to signal extraction

To estimate the systematic due to the signal extraction the following parameters were varied one by one:

#### Normalization range

In the standard procedure the mixed-event distribution was normalized to the same event distribution in the invariant mass region of  $1.1 < M < 1.2 \text{ GeV}/c^2$ . Two different normalization ranges were chosen for systematic study:  $1.1 - 1.4 \text{ GeV}/c^2$  and  $1.1 - 1.3 \text{ GeV}/c^2$ .

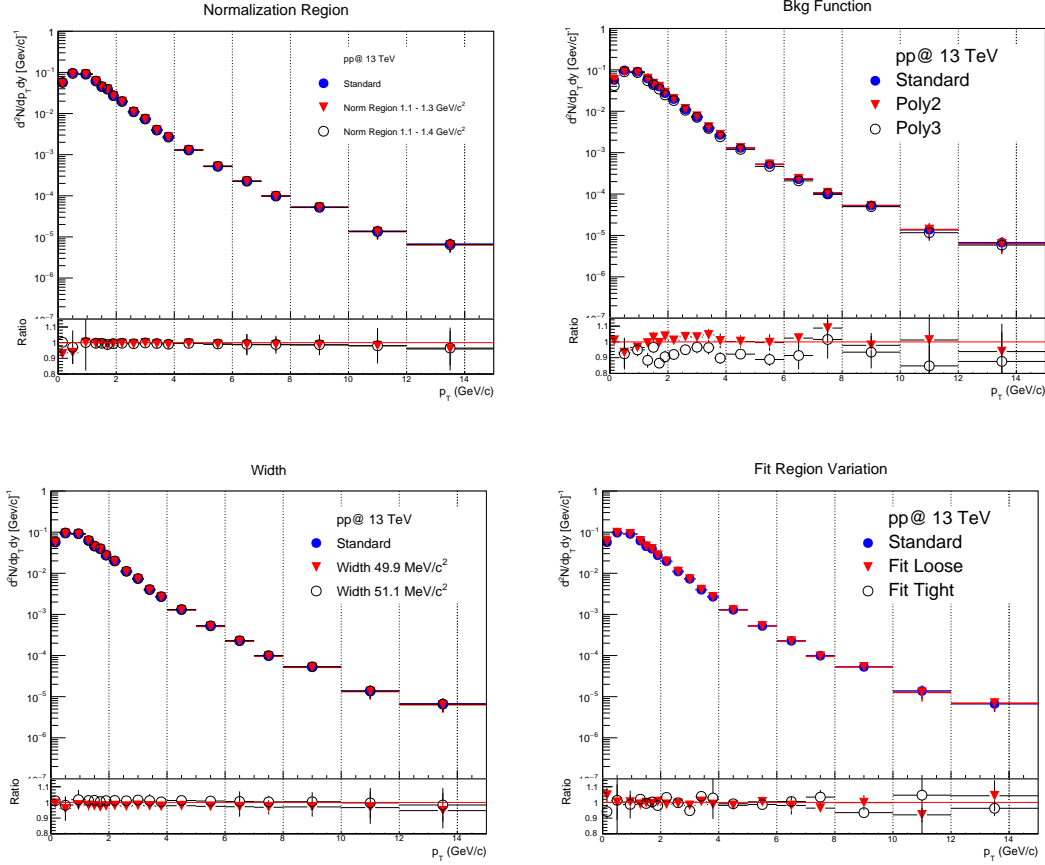


Fig. 13: Upper row:(Left panel) Comparison of standard  $p_T$  spectrum (blue circles) to  $p_T$  spectra obtained when the normalization region 1.1 - 1.4  $\text{GeV}/c^2$  (red triangles) or 1.1 - 1.3  $\text{GeV}/c^2$  (empty black circles) is used. (Right panel) Comparison of standard  $p_T$  spectrum (blue circles) to  $p_T$  spectra obtained when a 3rd (empty black circles) or a 2nd (red triangles) order polynomial is used to describe the residual background. Lower row: (Left panel) Comparison of standard  $p_T$  spectrum (blue circles) to  $p_T$  spectra obtained when for the fit the width is fixed to 49.9  $\text{MeV}/c^2$  (red triangles) or 51.7  $\text{MeV}/c^2$  (empty black circles). (Right panel) Comparison of standard  $p_T$  spectrum (blue circles) to  $p_T$  spectra obtained using a tight (empty black circles) or a loose (red triangles) fit region. In all the plots the ratios of the spectra obtained with the modified parameter to the standard one are shown in the lower panel.

In the left panel of upper row of Fig. 13 the  $p_T$  spectra obtained using these two new ranges are compared to the standard  $p_T$  spectrum. The ratios of the spectra obtained with the modified parameter to the standard one are shown in the lower panel.

### Residual background function

In the standard procedure the residual background was parameterized by the function 5. Only for the first  $p_T$  bin the residual background was parameterized by a first order polynomial. For systematic study two functions were used: 2nd and 3rd order polynomial.

In the right panel of upper row of Fig. 13 the  $p_T$  spectra obtained using a 2nd or a 3rd order polynomial for the residual background are compared to the standard  $p_T$  spectrum. The ratios of the spectra obtained with the modified parameter to the standard one are shown in the lower panel.

### Width

In the standard fit procedure the width of the non-relativistic Breit-Wigner was fixed to 50.8  $\text{MeV}/c^2$ ,

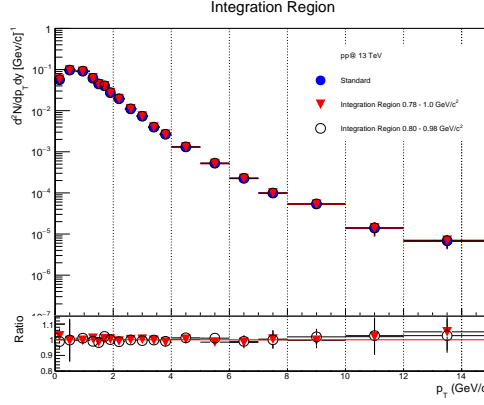


Fig. 14: Comparison of standard  $p_T$  spectrum (blue circles) to  $p_T$  spectra obtained using for the bin-counting the integration region 0.78 - 1.0  $GeV/c^2$  (red triangles) or 0.80 - 0.98  $GeV/c^2$  (empty black circles). The ratios of the spectra obtained with the modified parameter to the standard one are shown in the lower panel.

i.e. the PDG value expected for the  $K^*(892)^\pm$ . For systematic study the width was varied by the PDG uncertainty ( $\pm 0.9$   $MeV/c^2$ ). The fit results obtained with the width free are very poor and then this variation was not taken into account for the estimation of the systematics.

In the left panel of lower row of Fig. 13 the  $p_T$  spectra obtained using these two new widths are compared to the standard  $p_T$  spectrum. The ratios of the spectra obtained with the modified parameter to the standard one are shown in the lower panel.

### Fit region

The fit region  $[F_{low}, F_{high}]$  was chosen accurately for each  $p_T$  bins to improve the global  $\chi^2$  of the fit. For systematic study two different fit ranges were used:  $[F_{low}+0.050, F_{high}-0.050]$   $GeV/c^2$ (tight) and  $[0.65, F_{high}+0.050]$   $GeV/c^2$ (loose). For the first  $p_T$  bin the following fit ranges were used  $[F_{low}+0.020, F_{high}-0.020]$   $GeV/c^2$ (tight) and  $[0.65, F_{high}+0.020]$   $GeV/c^2$ (loose).

In the right panel of lower panel of Fig. 13 the  $p_T$  spectra obtained using these two new fit ranges are compared to the standard  $p_T$  spectrum. The ratios of the spectra obtained with the modified parameter to the standard one are shown in the lower panel.

### Extraction method

The raw yield was estimated using two different methods: the fit function or bin counting. The second method was used as default while the first for systematic study.

In Fig. 7 the raw yield  $p_T$  distributions obtained with the two methods are compared. The ratios of the spectra obtained with the modified parameter to the standard one are shown in the lower panel.

### Integration Region (for bin counting)

The standard range of the integration region for the bin counting was 0.79 - 0.99  $GeV/c^2$ . Two different regions were considered for the systematic estimation: 0.78 - 1.0  $GeV/c^2$  and 0.80 - 0.98  $GeV/c^2$ .

In Fig. 14 the  $p_T$  spectra obtained using these two new integration ranges are compared to the standard  $p_T$  spectrum. The ratios of the spectra obtained with the modified parameter to the standard one are shown in the lower panel.

To know if the observed yield variations are due to a systematic effect or to a statistical fluctuation Barlow check was performed. The distributions of  $\Delta/\sigma_{cc}$  obtained varying normalization region, residual

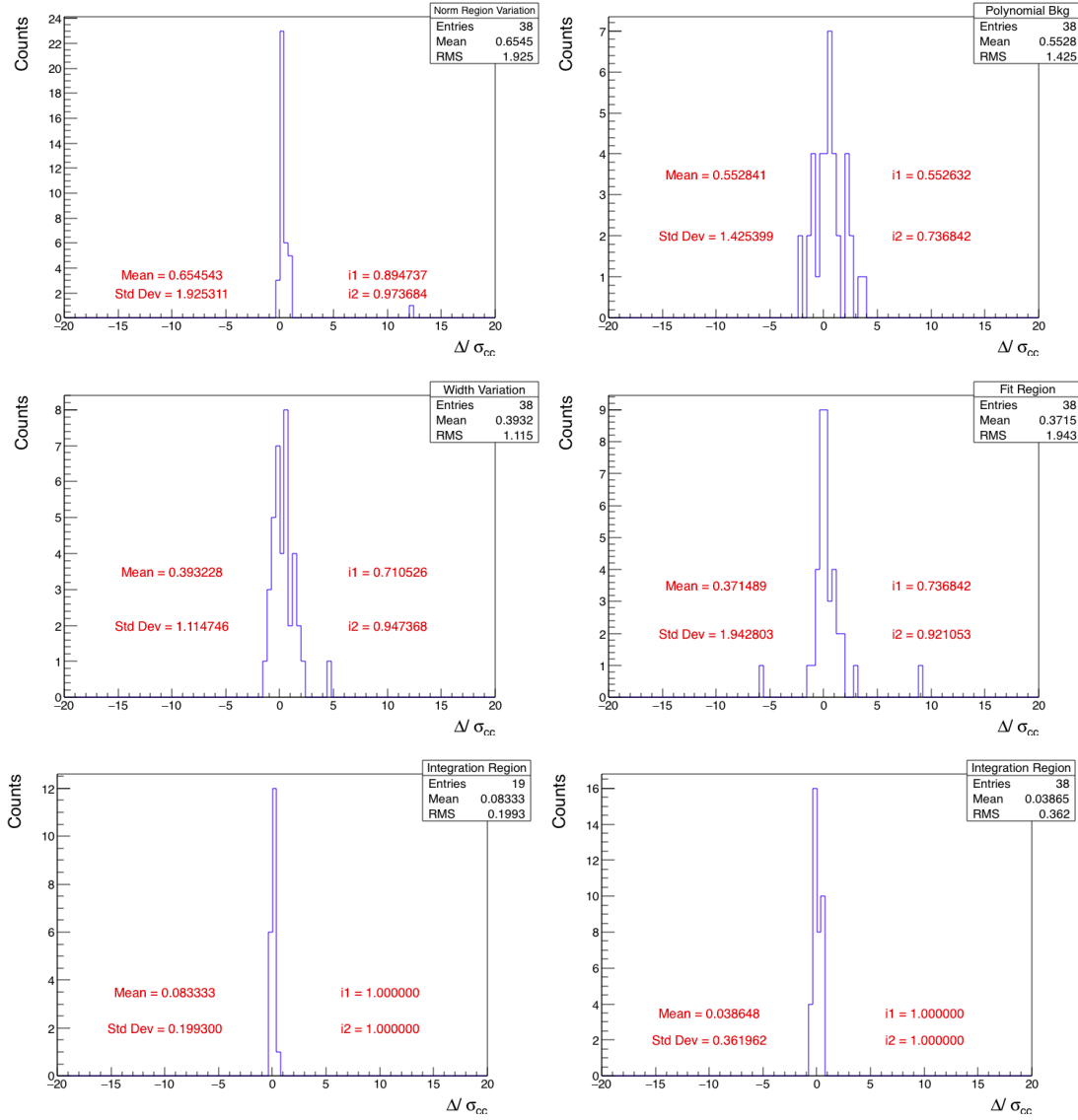


Fig. 15: Consistency check (Barlow check) for normalization region, residual background function, width, fit region, extraction method and integration region for bin-counting.  $I_1$  and  $I_2$  represent the percentage of entries within  $|\Delta/\sigma_{cc}| < 1$  and  $|\Delta/\sigma_{cc}| < 2$

background function, width, fit region, extraction method, integration region for bin-counting are shown in Fig. 15. Taking into account these consistency checks the variation of the yields due to the extraction method, to the integration region and to the width value were not used for the estimation of the systematic uncertainty of the signal extraction. Then for each  $p_T$  bin the systematic uncertainty for the signal extraction was obtained adding in quadrature the uncertainties due to the remaining four parameters (normalization region, residual background function, fit region).

#### 6.4 Systematic due to PID selection of primary tracks

The primary pions were identified through their energy loss  $dE/dx$  in the Time Projection Chamber (TPC) by  $p$ -dependent PID selection cuts described in Sect.3.1 (see Fig. 2). For systematic study PID cut  $|N\sigma_{TPC}| < 3.5$  and  $|N\sigma_{TPC}| < 2.5$  were used.

In the left panel of Fig. 16 the  $p_T$  spectra obtained using these two new PID cuts are compared to the standard  $p_T$  spectrum. The ratios of the spectra obtained with the modified parameter to the standard one

are shown in the lower panel.

The  $\Delta/\sigma_{cc}$  distribution for the PID cut variations is shown in the right panel of Fig. 16. From this consistency check the observed variations are statistically significant then for each  $p_T$  bin the systematic uncertainty for the PID cut was given from the largest measured variation.

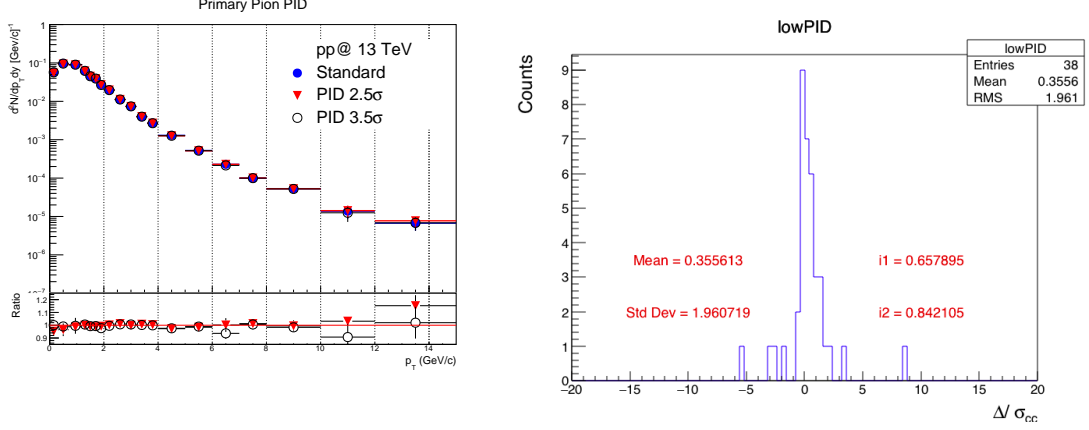


Fig. 16: (Left panel) Comparison of standard  $p_T$  spectrum (blue circles) to  $p_T$  spectra obtained identifying primary pions by a  $|\mathbf{N}\sigma_{\text{TPC}}| < 3.5$  (empty black circles) or a  $|\mathbf{N}\sigma_{\text{TPC}}| < 2.5$  (red triangles) PID cut. The ratios of the spectra obtained with the modified parameter to the standard one are shown in the lower panel. (Right panel) Consistency check (Barlow check) for primary pions PID cuts.

### 6.5 Systematic due to secondary tracks selection + PID cuts

To estimate the systematic due to the secondary track selection the following parameters were varied one by one using the maximum variation adopted for studying  $K_S^0$  systematics in pp collisions at  $\sqrt{s} = 13$  TeV [2]:

#### Minimum number of rows crossed in TPC

In the standard cut set the minimum number of rows crossed in TPC for the secondary tracks is  $> 70$  ( $N_{\text{TPC}_{\text{row}}} > 70$ ). One variation was considered for the systematic study:  $N_{\text{TPC}_{\text{row}}} > 100$ .

In the left panel of the upper row of Fig. 17 the  $p_T$  spectrum obtained for  $N_{\text{TPC}_{\text{row}}} > 100$  is compared to the standard  $p_T$  spectrum. The ratio of the spectrum obtained with the modified parameter to the standard one is shown in the lower panel.

#### Ratio of number of crossed rows to number of findable clusters in TPC

In the standard cut set for the secondary tracks the ratio of number of crossed rows to number of findable clusters in TPC should be  $> 0.8$  ( $N_{\text{TPC}_{\text{row}}}/\text{clusters} > 0.8$ ). One variation was considered for the systematic study:  $N_{\text{TPC}_{\text{row}}}/\text{clusters} > 0.9$ .

In the right panel of the upper row of Fig. 17 the  $p_T$  spectrum obtained for  $N_{\text{TPC}_{\text{row}}}/\text{clusters} > 0.9$  is compared to the standard  $p_T$  spectrum. The ratio of the spectrum obtained with the modified parameter to the standard one is shown in the lower panel.

#### TPC $\chi^2/\text{clusters}$

In the standard cut set for the secondary tracks the TPC  $\chi^2/\text{clusters}$  should be  $< 4.0$ . One variation was considered for the systematic study:  $\chi^2/\text{clusters} < 2.3$ .

In the left panel of lower row of Fig. 17 the  $p_T$  spectrum obtained for  $\chi^2/\text{clusters} < 2.3$  is compared to the standard  $p_T$  spectrum. The ratio of the spectrum obtained with the modified parameter to the standard one is shown in the lower panel.

#### DCA of secondary tracks to PV

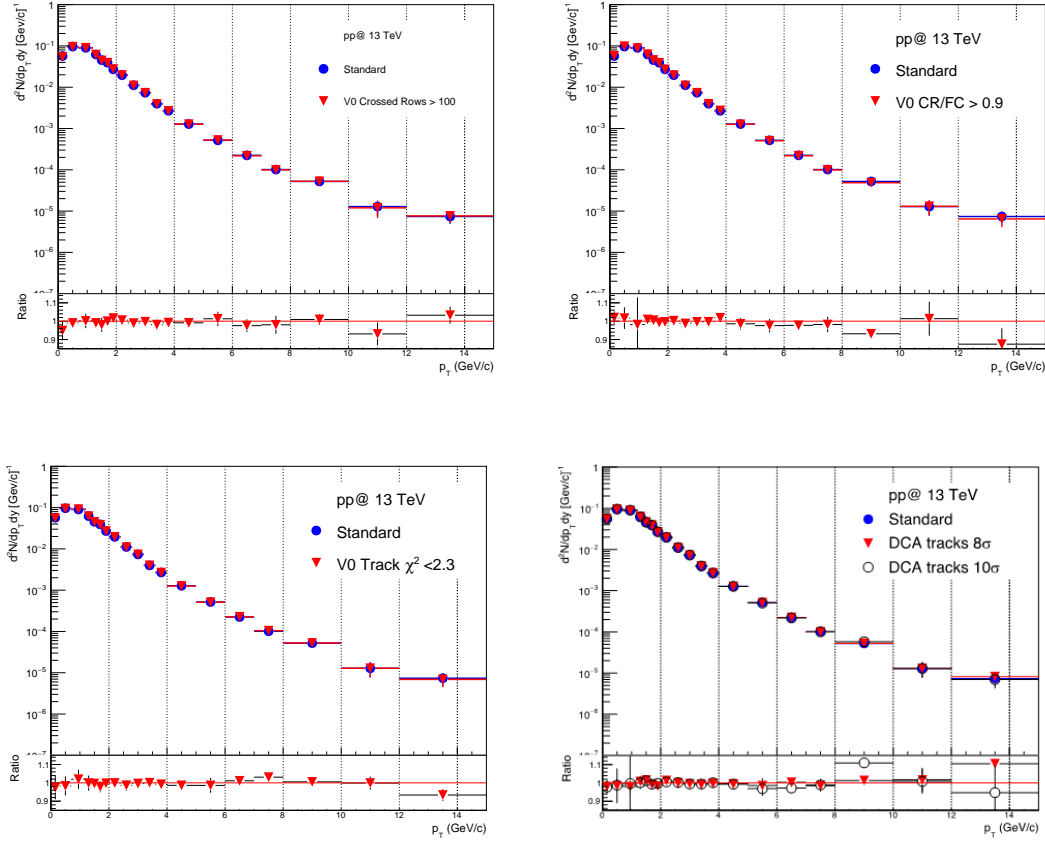


Fig. 17: Upper row: (Left panel) Comparison of standard  $p_T$  spectrum (blue circles) to  $p_T$  spectrum obtained for  $N_{TPCrows} > 100$  (red triangles). (Right panel) Comparison of standard  $p_T$  spectrum (blue circles) to  $p_T$  spectrum obtained for  $N_{TPCrows}/clusters > 0.9$  (red triangles). Lower row: (Left panel) Comparison of standard  $p_T$  spectrum (blue circles) to  $p_T$  spectrum obtained for  $\chi^2/clusters < 2.3$  (red triangles). (Right panel) Comparison of standard  $p_T$  spectrum (blue circles) to  $p_T$  spectra obtained for  $DCA_r > 8 \sigma$  (empty black circles) and  $DCA_r > 10 \sigma$  (red triangles). In all the plots the ratios of the spectra obtained with the modified parameter to the standard one are shown in the lower panel.

In the standard cut set for the secondary tracks the DCA to primary vertex should be  $> 0.0105 + 0.0350 p_T^{-1.1}$  cm, i.e.  $DCA_r > 7 \sigma$ . Two variations were considered for the systematic study:  $8 \sigma$  and  $10 \sigma$ .

In the right panel of lower row of Fig. 17 the  $p_T$  spectra obtained for  $DCA_r > 8 \sigma$  and  $DCA_r > 10 \sigma$  cut are compared to the standard  $p_T$  spectrum. The ratios of the spectra obtained with the modified parameter to the standard one are shown in the lower panel.

### PID for secondary pions

In the standard set cut the secondary pions of the  $K_S^0$  decay were identified by a  $5\sigma_{TPC}$  PID cut ( $|N\sigma_{TPC}| < 5$ ). Two variations were considered for the systematic study:  $4\sigma_{TPC}$  and  $4.5\sigma_{TPC}$ .

In the left panel of Fig. ?? the  $p_T$  spectra obtained for  $|N\sigma_{TPC}| < 4$  and  $|N\sigma_{TPC}| < 4.5$  are compared to the standard  $p_T$  spectrum. The ratios of the spectra obtained with the modified parameter to the standard one are shown in the lower panel.

Taking into account the results of the consistency check done for the previous described parameters (see Fig. ?? and right panel of Fig. ??) the all the observed variations are not due to a systematical effect.

## 6.6 Systematic due to topological cuts for $V^0$ selection

To estimate the systematic due to the  $V^0$  selection the following parameters were varied one by one using the maximum and minimum variation adopted for studying  $K_S^0$  systematics in pp collisions at  $\sqrt{s} = 13$  TeV [2]:

### Fiducial Volume ( $V^0$ 2D decay radius)

In the standard cut set the  $V^0$  2D decay radius is  $> 0.5$  cm ( $R > 0.5$  cm). Two variations were considered for the systematic study: 0.3 and 0.7 cm.

In the left panel of the upper row of Fig. 20 the  $p_T$  spectra obtained for  $R > 0.3$  cm and  $R > 0.7$  cm are compared to the standard  $p_T$  spectrum. The ratios of the spectra obtained with the modified parameter to the standard one are shown in the lower panel.

### Cosine of pointing angle

In the standard cut set  $V^0$  cosine of pointing angle is  $> 0.97$  ( $\cos(\theta_{pointing}) > 0.97$ ). Two variations were considered for the systematic study: 0.95 and 0.99.

In the right panel of the upper row of Fig. 20 the  $p_T$  spectra obtained for  $\cos(\theta_{pointing}) > 0.95$  and  $\cos(\theta_{pointing}) > 0.99$  are compared to the standard  $p_T$  spectrum. The ratios of the spectra obtained with the modified parameter to the standard one are shown in the lower panel.

### DCA $V^0$ daughters

In the standard cut set the DCA between the  $V^0$  daughters is  $< 1.0 \sigma$  ( $DCA(V^0) < 1.0 \sigma$ ). Two variations were considered for the systematic study:  $0.75 \sigma$  and  $1.25 \sigma$ .

In the left panel of the middle row of Fig. 20 the  $p_T$  spectra obtained for  $DCA(V^0) < 0.75 \sigma$  and  $DCA(V^0) < 1.25 \sigma$  are compared to the standard  $p_T$  spectrum. The ratios of the spectra obtained with the modified parameter to the standard one are shown in the lower panel.

### $V^0$ mass tolerance

In the standard cut set the  $V^0$  is identified by mass cut  $\left| M_{K_S^0} - 497.611 \right| < 30 \text{ MeV}/c^2$  ( $\Delta M < 30 \text{ MeV}/c^2$ ). Two variations were considered for the systematic study:  $20 \text{ MeV}/c^2$  and  $40 \text{ MeV}/c^2$ .

In the right panel of the middle row of Fig. 20 the  $p_T$  spectra obtained for  $\left| M_{K_S^0} - 497.611 \right| < 20 \text{ MeV}/c^2$  and  $\left| M_{K_S^0} - 497.611 \right| < 40 \text{ MeV}/c^2$  are compared to the standard  $p_T$  spectrum. The ratios of the spectra obtained with the modified parameter to the standard one are shown in the lower panel.

### $V^0$ lifetime

In the standard cut set the lifetime of the  $V^0$  ( $mL/p$ ) is  $< 20$  cm ( $\tau < 20$  cm). A variation was considered for the systematic study:  $\tau < 12$  cm

In the left panel of the lower row of Fig. 20 the  $p_T$  spectrum obtained for  $\tau < 12$  cm is compared to the standard  $p_T$  spectrum. The ratio of the spectrum obtained with the modified parameter to the standard one is shown in the lower panel.

### DCA $V^0$ to Primary Vertex

In the standard cut set the DCA of the  $V^0$  to the primary vertex is  $< 0.3$  cm. Two variations were considered for the systematic study: 0.2 cm and 0.4 cm.

In the right panel of the lower row of Fig. 20 the  $p_T$  spectra obtained for  $DCA(PV) < 0.2$  cm and

DCA(PV)  $< 0.4$  cm are compared to the standard  $p_T$  spectrum. The ratios of the spectra obtained with the modified parameter to the standard one are shown in the lower panel.

Taking into account the results of the consistency check done for the previous described parameters (see Fig. 21) only the variations of 1) Cosine of pointing angle, 2) DCA  $V^0$  to PV are due to a systematical effect. Then for each  $p_T$  bin the systematic uncertainty for the  $V^0$  extraction was obtained adding in quadrature the uncertainties due to these cuts.

## 6.7 Systematic due to primary track selection

### 6.7.1 Primary track cuts

The systematic uncertainty due to the primary track selection were estimated by changing the following parameter one by one using the same variation adopted for studying  $K^{*0}$  systematics in pp collisions at  $\sqrt{s} = 13$  TeV [1]:

#### Minimum number of rows crossed in TPC

In the standard cut set for the primary track selection the minimum number of rows crossed in TPC is  $> 70$  ( $N_{TPC_{row}} > 70$ ). Two variations were considered for the systematic study:  $N_{TPC_{row}} > 80$  and  $N_{TPC_{row}} > 100$ .

In the left panel of the upper row of Fig. 22 the  $p_T$  spectra obtained for  $N_{TPC_{row}} > 80$  and  $N_{TPC_{row}} > 100$  are compared to the standard  $p_T$  spectrum. The ratios of the spectra obtained with the modified parameter to the standard one are shown in the lower panel.

#### Ratio of number of crossed rows to number of findable clusters in TPC

In the standard cut set for the primary track selection the ratio of number of crossed rows to number of findable clusters in TPC is  $> 0.8$  ( $N_{TPC_{row}}/clusters > 0.8$ ). One variation was considered for the systematic study:  $N_{TPC_{row}}/clusters > 0.9$ .

In the right panel of the upper row of Fig. 22 the  $p_T$  spectrum obtained for  $N_{TPC_{row}}/clusters > 0.9$  is compared to the standard  $p_T$  spectrum. The ratio of the spectrum obtained with the modified parameter to the standard one is shown in the lower panel.

#### TPC $\chi^2/clusters$

In the standard cut set for the primary tracks the TPC  $\chi^2/clusters$  is  $< 4.0$ . One variation was considered for the systematic study:  $\chi^2/clusters < 2.3$ .

In the left panel of the lower row of Fig. 22 the  $p_T$  spectrum obtained for  $\chi^2/clusters < 2.3$  is compared to the standard  $p_T$  spectrum. The ratio of the spectrum obtained with the modified parameter to the standard one is shown in the lower panel.

#### ITS $\chi^2/clusters$

In the standard cut set for the primary tracks the ITS  $\chi^2/clusters$  is  $< 36.0$ . Two variations were considered for the systematic study:  $\chi^2/clusters < 4$  and  $\chi^2/clusters < 25$ .

In the left panel of the lower panel of Fig. 22 the  $p_T$  spectra obtained for  $\chi^2/clusters < 4$  and  $\chi^2/clusters < 25$  are compared to the standard  $p_T$  spectrum. The ratios of the spectra obtained with the modified parameter to the standard one are shown in the lower panel.

#### ITS-TPC global $\chi^2/clusters$

In the standard cut set for the primary tracks the TPC-global tracking is  $\chi^2/clusters < 36.0$ . One variation was considered for the systematic study:  $\chi^2/clusters < 25$ .



In the left panel of the upper row of Fig. 23 the  $p_T$  spectrum obtained for  $\chi^2/\text{clusters} < 25$  is compared to the standard  $p_T$  spectrum. The ratio of the spectrum obtained with the modified parameter to the standard one is shown in the lower panel.

#### Minimum number of SPD cluster

In the standard cut set for the primary tracks the minimum number of cluster in the SPD is equal to 1 ( $kSPD \geq 1$ ). One variation was considered for the systematic study:  $kSPD \geq 0$ .

In the right panel of the upper row Fig. 23 the  $p_T$  spectrum obtained for  $kSPD \geq 0$  is compared to the standard  $p_T$  spectrum. The ratio of the spectrum obtained with the modified parameter to the standard one is shown in the lower panel.

#### Longitudinal impact parameter

In the standard cut set for the primary tracks the longitudinal impact parameter  $DCA_z$  is  $< 2$  cm. Two variations were considered for the systematic study:  $DCA_z < 0.2$  cm and  $DCA_z < 1.0$  cm.

In the left panel of the lower row of Fig. 23 the  $p_T$  spectrum obtained for  $DCA_z < 0.2$  cm and  $DCA_z < 1.0$  cm are compared to the standard  $p_T$  spectrum. The ratios of the spectra obtained with the modified parameter to the standard one are shown in the lower panel.

#### Radial impact parameter

In the standard cut set for the primary tracks the radial impact parameter  $DCA_r$  is  $< 7\sigma$ . One variations was considered for the systematic study:  $DCA_r < 4\sigma$ .

In the right panel of the lower row of Fig. 23 the  $p_T$  spectrum obtained for  $DCA_r < 4\sigma$  is compared to the standard  $p_T$  spectrum. The ratio of the spectrum obtained with the modified parameter to the standard one is shown in the lower panel.

Taking into account the results of the consistency check done for the previous described parameters (see Fig. ??) only the variations of ratio of number of crossed rows, TPC  $\chi^2/\text{clusters}$ , ITS-TPC global  $\chi^2/\text{clusters}$ , are due to a systematical effect. Then for each  $p_T$  bin the systematic uncertainty for the primary track estimation was obtained adding in quadrature the uncertainties due to these cuts.

#### 6.7.2 Global tracking

The tracking uncertainty, due to the uncertainty in ITS-TPC matching, was derived for the  $K^*(892)^\pm$  as follows. The one-particle uncertainty  $u(p_{T\pi^\pm})$  was inherited from the analysis of unidentified charged hadron production in the same collision system [8]. A PYTHIA simulation (the LHC15g3a3 production) was used to find the  $p_T$  distributions of the primary pion of the  $K^*(892)^\pm$  decay of the different  $p_T$  bins of the  $K^*(892)^\pm$  transverse momentum. These  $p_T$  distributions ( $p_T(\pi^\pm)$ ) were then used to obtain the weighted average of the tracking uncertainty for each  $K^*(892)^\pm$  transverse-momentum bin.

The global tracking uncertainty is the ratio of two histograms (a weighted average): Numerator: the sum, for all generated  $K^{*\pm}$  mesons, of  $N(p_{TK^{*\pm}}, p_{T\pi^\pm}) \times w(p_{TK^{*\pm}}) \times u(p_{T\pi^\pm})$  Denominator: the sum, for all generated  $K^{*\pm}$  mesons, of  $N(p_{TK^{*\pm}}, p_{T\pi^\pm}) \times w(p_{TK^{*\pm}})$ .

The distribution of the uncertainty due to the global tracking as a function of  $p_T$  is shown in Fig. 25.

#### 6.8 Systematic due to primary vertex selection

This systematic uncertainty takes into account for the differences observed in the yield due to variations in the  $z$  position cut of the primary vertex. In the standad event cut set  $|v_z| < 10$  cm. Two variations were considered for the systematic study:  $|v_z| < 8$  cm and  $|v_z| < 12$  cm.

In the left panel of Fig. 26 the  $p_T$  spectrum obtained for  $|v_z| < 12$  cm and  $|v_z| < 8$  cm are compared to

the standard  $p_T$  spectrum. The ratios of the spectra obtained with the modified parameter to the standard one are shown in the lower panel.

The  $\Delta/\sigma_{cc}$  distribution for the primary vertex cut variations is shown in the right panel of Fig. 26. Mean and standard deviation are as expected for 'normal' distribution then no systematic uncertainty was considered for this cut.

### 6.9 Systematic due to material budget

The systematic uncertainty due to uncertainties in the ALICE material budget was taken from the analysis of the  $K^*(892)^0$  mesons in p-Pb collisions [9]. It is  $p_T$ -dependent and reaches a maximum value of a few percent.  $\sigma_{mat} = 1.2\%$  for  $0 < p_T < 4$  GeV/c and  $< 0.5\%$  for  $p_T > 4$  GeV/c.

### 6.10 Systematic due to hadronic interactions

The systematic uncertainty due to hadronic interaction was taken from the analysis of the  $K^*(892)^0$  mesons in p-Pb collisions [9]. It is  $p_T$ -dependent and reaches a maximum value of a few percent.  $\sigma_{hadronic} = 1.9\%$  for  $0 < p_T < 4$  GeV/c and  $< 0.5\%$  for  $p_T > 4$  GeV/c.

### 6.11 Total systematic uncertainty

The systematic uncertainties from different sources were added in quadrature to obtain the total systematic uncertainty. The  $p_T$  distributions of the systematic uncertainty of the different sources previously described are shown in Fig. 27. In the same figure the  $p_T$  distribution of the total systematic uncertainty estimated for the  $K^*(892)^\pm$  production in pp collisions at  $\sqrt{s} = 13$  TeV is also shown. The mean uncertainties are: Signal Extraction (8.2 %), Topological cuts (3.9 %), Primary Pions PID (2.6 %), Signal Loss correction (0.3 %), Primary Tracks (2.6 %), Global Tracking (3.3 %), INEL Normalization (2.5 %).

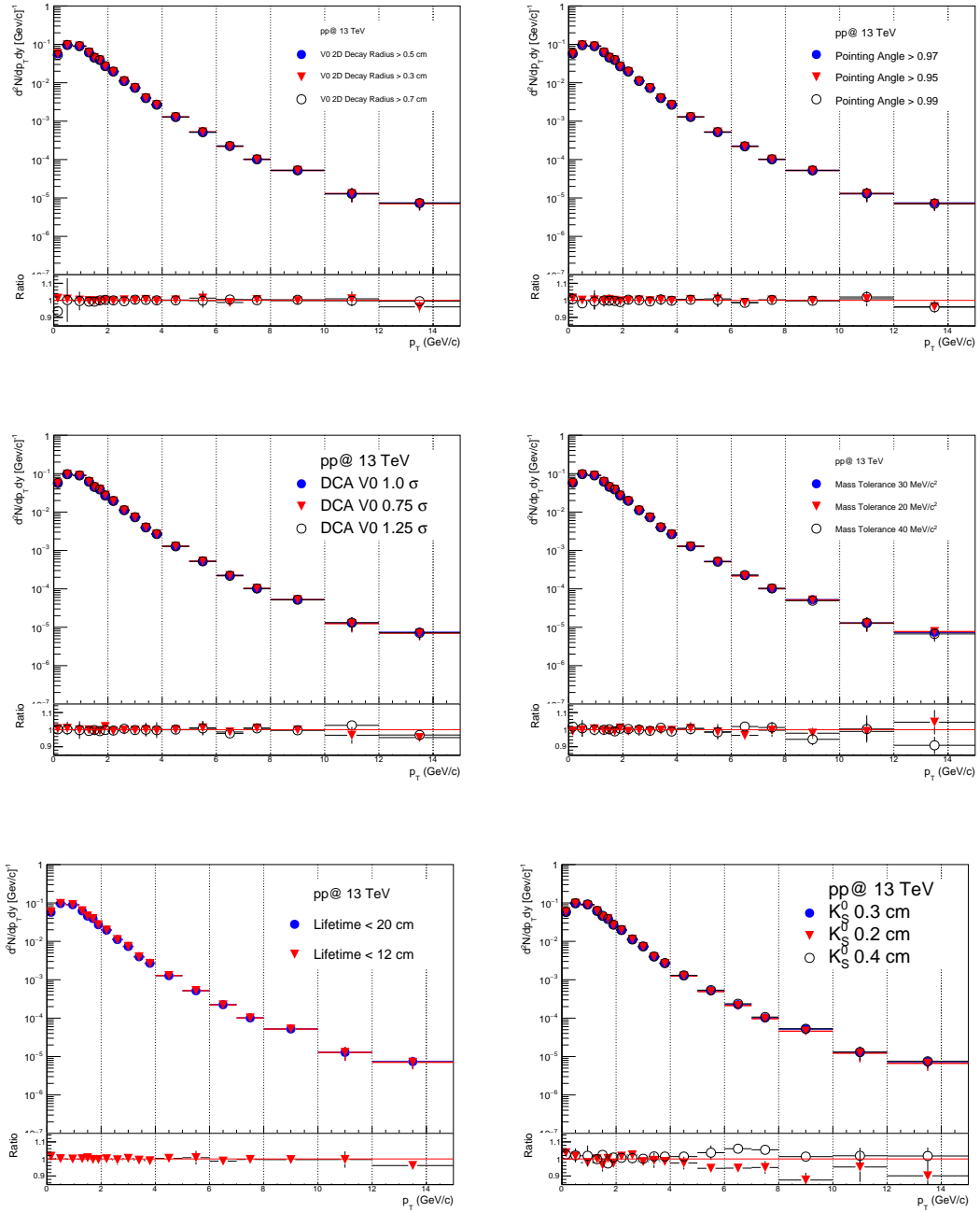


Fig. 20: Upper row: (Left panel) Comparison of standard  $p_T$  spectrum (blue circles) to  $p_T$  spectra obtained for  $R > 0.3$  cm (empty black circles) and  $R > 0.7$  cm (red triangles). (Right panel) Comparison of standard  $p_T$  spectrum (blue circles) to  $p_T$  spectra obtained for  $\cos(\theta_{\text{pointing}}) > 0.95$  (empty black circles) and  $\cos(\theta_{\text{pointing}}) > 0.99$  (red triangles). Middle row: (Left panel) Comparison of standard  $p_T$  spectrum (blue circles) to  $p_T$  spectra obtained for  $\text{DCA}(V^0) < 0.75 \sigma$  (empty black circles) and  $\text{DCA}(V^0) < 1.25 \sigma$  (red triangles). (Right panel) Comparison of standard  $p_T$  spectrum (blue circles) to  $p_T$  spectra obtained for  $\Delta M < 20 \text{ MeV}/c^2$  (empty black circles) and  $\Delta M < 40 \text{ MeV}/c^2$  (red triangles). Lower row: (Left panel) Comparison of standard  $p_T$  spectrum (blue circles) to  $p_T$  spectra obtained for  $\tau < 12$  cm (red triangles). (Right panel) Comparison of standard  $p_T$  spectrum (blue circles) to  $p_T$  spectra obtained for  $\text{DCA}(\text{PV}) < 0.2$  (red triangles) and  $\text{DCA}(\text{PV}) < 0.4$  (empty black circles). For all the plots the ratios of the spectra obtained with the modified parameter to the standard one are shown in the lower panel.

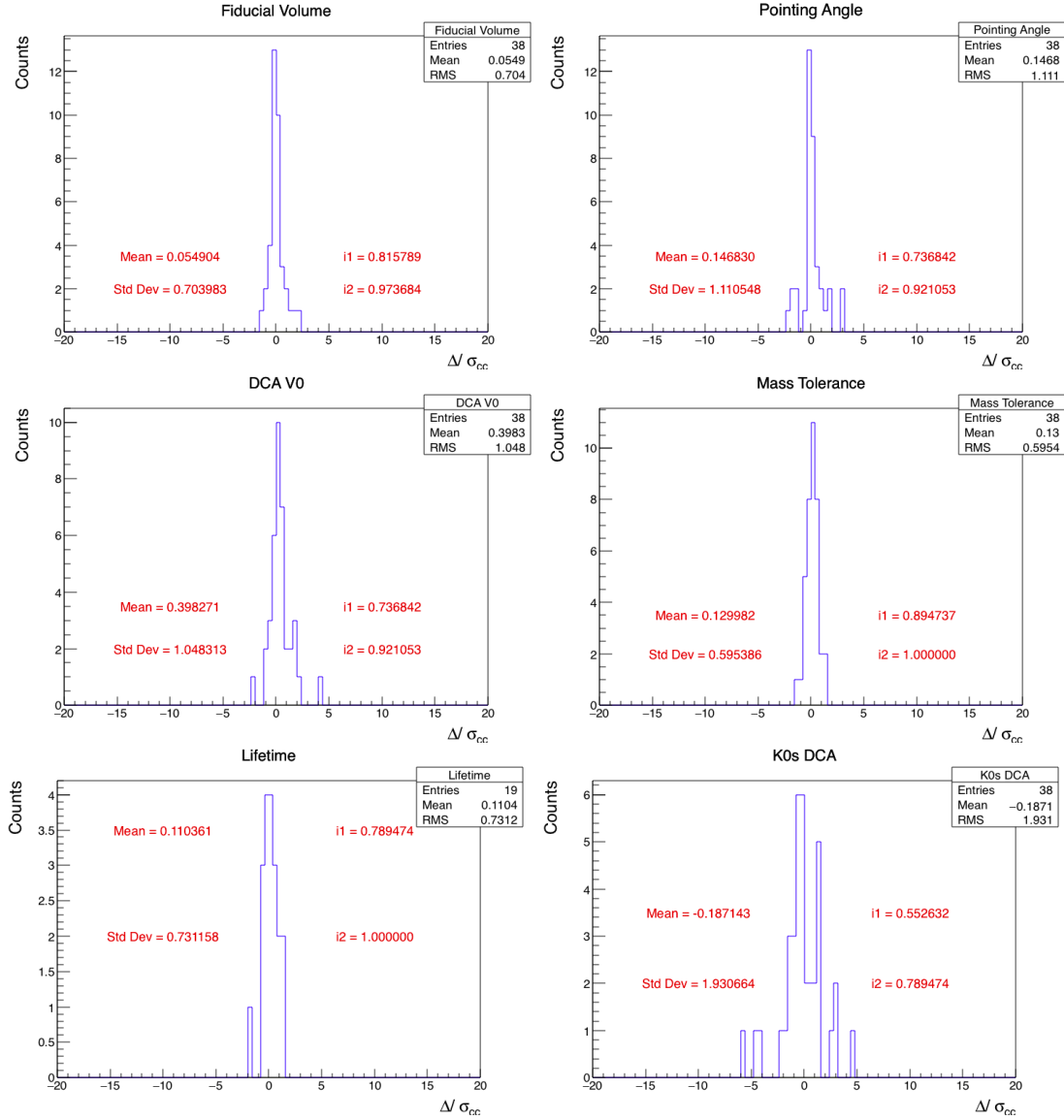


Fig. 21: Consistency check (Barlow check) for  $V^0$  extraction cut: 2D decay radius, cosine of pointing angle, DCA  $V^0$  daughters, mass tolerance, lifetime, DCA of  $V^0$  to PV.  $I_1$  and  $I_2$  represent the percentage of entries within  $|\Delta/\sigma_{cc}| < 1$  and  $|\Delta/\sigma_{cc}| < 2$

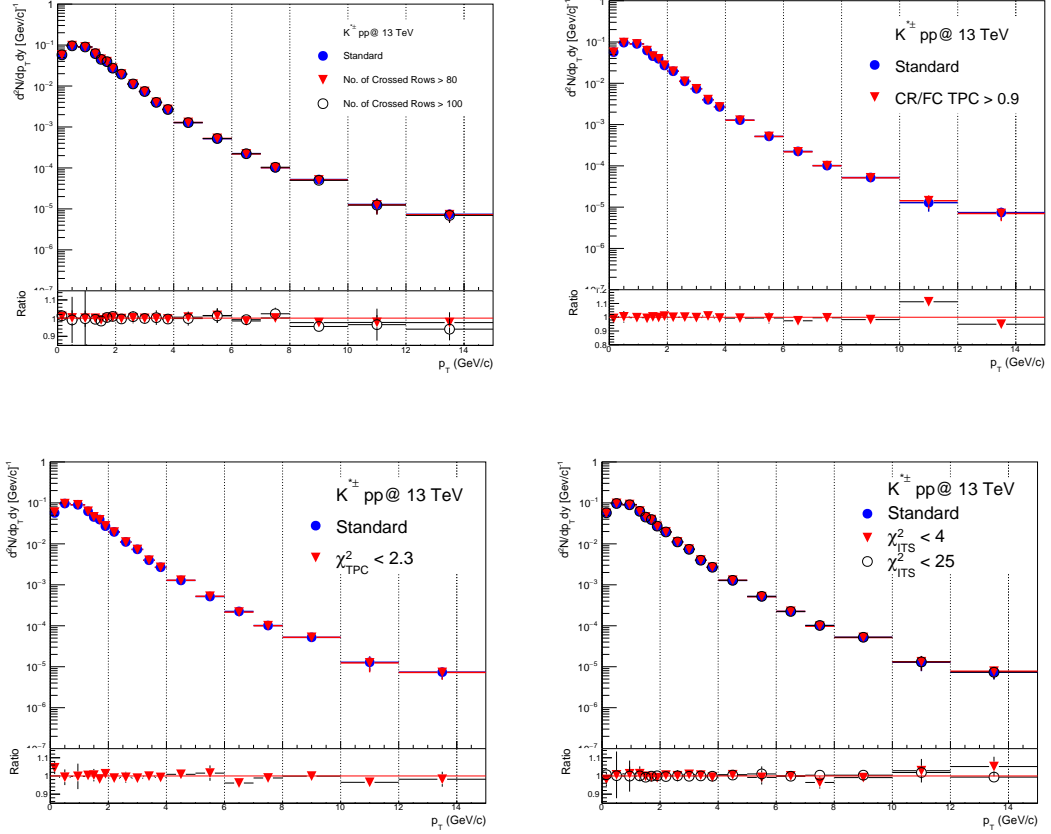


Fig. 22: Upper row: (Left panel) Comparison of standard  $p_T$  spectrum (blue circles) to  $p_T$  spectrum obtained for  $N_{TPC_{row}} > 80$  (red triangles) and  $N_{TPC_{row}} > 100$  (empty black circles) for primary tracks. (Right panel) Comparison of standard  $p_T$  spectrum (blue circles) to  $p_T$  spectrum obtained for  $N_{TPC_{row}}/clusters > 0.9$  (red triangles) for primary tracks. Lower row: (Left panel) Comparison of standard  $p_T$  spectrum (blue circles) to  $p_T$  spectrum obtained for  $TPC \chi^2/clusters < 2.3$  (red triangles) for primary tracks. (Right panel) Comparison of standard  $p_T$  spectrum (blue circles) to  $p_T$  spectrum obtained for  $ITS \chi^2/clusters < 4$  (red triangles) and  $ITS \chi^2/clusters < 25$  (empty black circles) for primary tracks. In all the plots the ratios of the spectra obtained with the modified parameter to the standard one are shown in the lower panel.

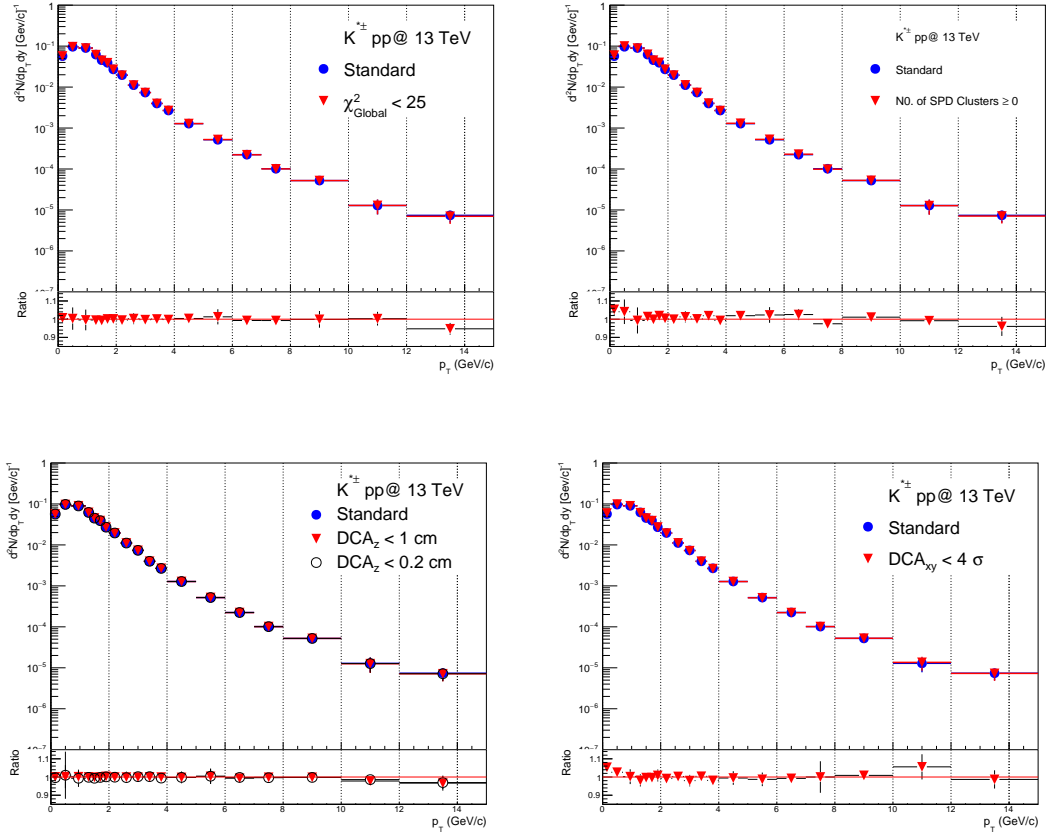


Fig. 23: Upper panel: (Left panel) Comparison of standard  $p_T$  spectrum (blue circles) to  $p_T$  spectrum obtained for TPC-global tracking  $\chi^2/\text{clusters} < 25$  (red triangles). (Right panel) Comparison of standard  $p_T$  spectrum (blue circles) to  $p_T$  spectrum obtained for kSPD  $\geq 0$  (red triangles). Lower panel: (Left panel) Comparison of standard  $p_T$  spectrum (blue circles) to  $p_T$  spectrum obtained for longitudinal impact parameter  $DCA_z < 0.2$  cm (empty black circles) and  $DCA_z < 1.0$  cm (red triangles). (Right panel) Comparison of standard  $p_T$  spectrum (blue circles) to  $p_T$  spectrum obtained for  $DCA_r < 4\sigma$  (red triangles). For all the plots the ratio of the spectra obtained with the modified parameter to the standard one are shown in the lower panel.

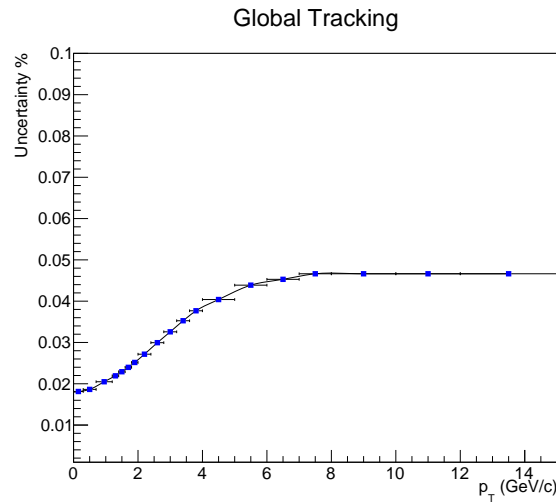


Fig. 25: Tracking (ITS-TPC Matching) efficiency uncertainty for the  $K^{*\pm}$

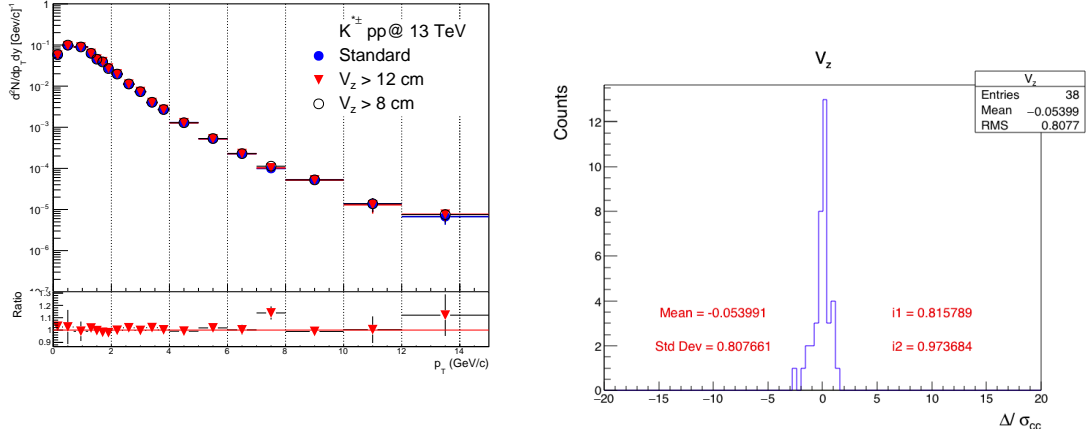


Fig. 26: (Left panel) Comparison of standard  $p_T$  spectrum (blue circles) to  $p_T$  spectra obtained for  $|v_z| < 12$  cm (red triangles) and  $|v_z| < 8$  cm (empty black circles). The ratios of the spectra obtained with the modified parameter to the standard one are shown in the lower panel. (Right panel) Consistency check (Barlow check) for primary vertex cut.  $I_1$  and  $I_2$  represent the percentage of entries within  $|\Delta/\sigma_{cc}| < 1$  and  $|\Delta/\sigma_{cc}| < 2$

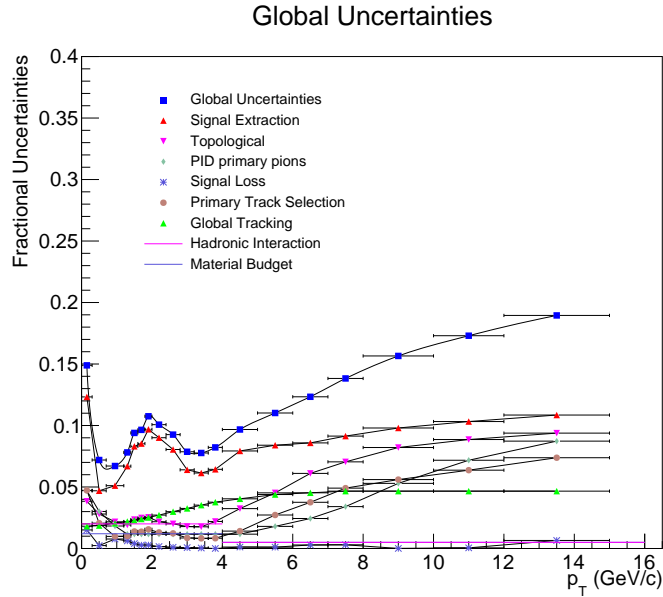


Fig. 27: The  $p_T$  distributions of the systematic uncertainty of the different sources (see text) are shown by lines of different colors. The  $p_T$  distribution of the total systematic uncertainty estimated for the  $K^*(892)^{\pm}$  production in pp collisions at  $\sqrt{s} = 13$  TeV is also shown.

## 7 Results

### 7.1 Corrected $p_T$ spectrum

To extract the inelastic yield, raw counts were corrected for: 1) the decay branching ratio (BR), 2) the trigger losses ( $\epsilon_{SL}$ ), 3) geometrical acceptance and detector efficiency ( $\epsilon_{rec}$ ), 4) the efficiency for trigger selection for inelastic pp collisions ( $f_{norm}$ ), 5) the signal loss introduced by the requirement to reconstruct a primary vertex ( $f_{vertex}$ ). The inelastic yield was estimated by the following formula:

$$\frac{d^2N}{dp_T dy} = \frac{\text{RawCounts}}{N_{MB} \times BR \times \Delta p_T \times \Delta y} \frac{\epsilon_{SL}}{\epsilon_{rec}} \times f_{norm} \times f_{vertex} \quad (13)$$

where  $\Delta y = 1$ ,  $N_{MB}$  is the number of the minimum bias trigger selected by the event cuts,  $BR = 0.66 \times 0.5 = 0.33$  is the branching ratio in  $K_S^0 + \pi^\pm$ ,  $\epsilon_{rec}$  is the weighted acceptance  $\times$  efficiency. The signal-loss correction  $\epsilon_{SL}$  accounts for the loss of  $K^*(892)^\pm$  mesons incurred by selecting events that satisfy the kINT7 trigger, rather than all inelastic events. It is a small  $p_T$  dependent factor, see paragraph 5.3 The inelastic normalization factor is  $f_{norm} = 0.7448 \pm 0.019$  [10], it takes into account the efficiency for trigger selection for inelastic pp collisions. The factor  $f_{vertex} = 0.931264$  [10] accounts for the signal loss introduced by the requirement that a primary vertex must be reconstructed. It is given by a ratio with Denominator: the number of triggered events (after application of the IsIncompleteDAQ cut and the pileup cuts); Numerator: the subset of the events in the denominator for which a good vertex was found (i.e., it passes the vertex quality cuts, but without the cut on the z-position of the vertex).

The obtained inelastic  $p_T$  spectrum for  $K^*(892)^\pm$  is shown in Fig. 28.

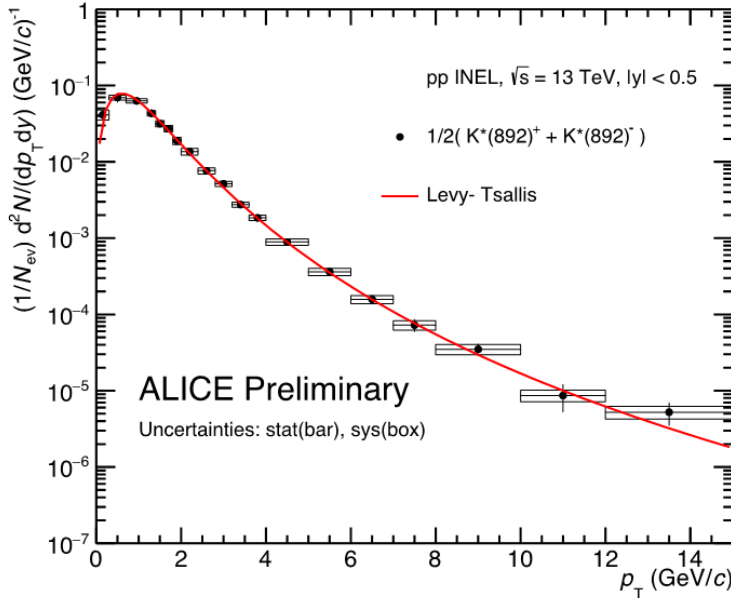


Fig. 28: Inelastic  $K^*(892)^\pm$  spectrum at mid-rapidity in pp collisions at  $\sqrt{s} = 13$  TeV with Levy-Tsallis fit (red curve) Statistical (bars) and systematics (boxes) uncertainties are also reported.

### 7.2 Comparison with $K^*(892)^0$ $p_T$ spectrum

In Fig. 29 the  $p_T$  spectrum (without  $f_{vertex} \times f_{norm}$  and signal-loss correction) of  $K^*(892)^\pm$  is compared with the  $K^*(892)^0$  one [1]. A very good agreement is observed between the  $p_T$  spectra of charged and



neutral  $K^*(892)$  resonance. In the right panel of Fig. 29 for the  $K^*(892)^0$  spectrum the same binning of  $K^*(892)^\pm$  was used to permit to estimate the ratio between the two spectra.

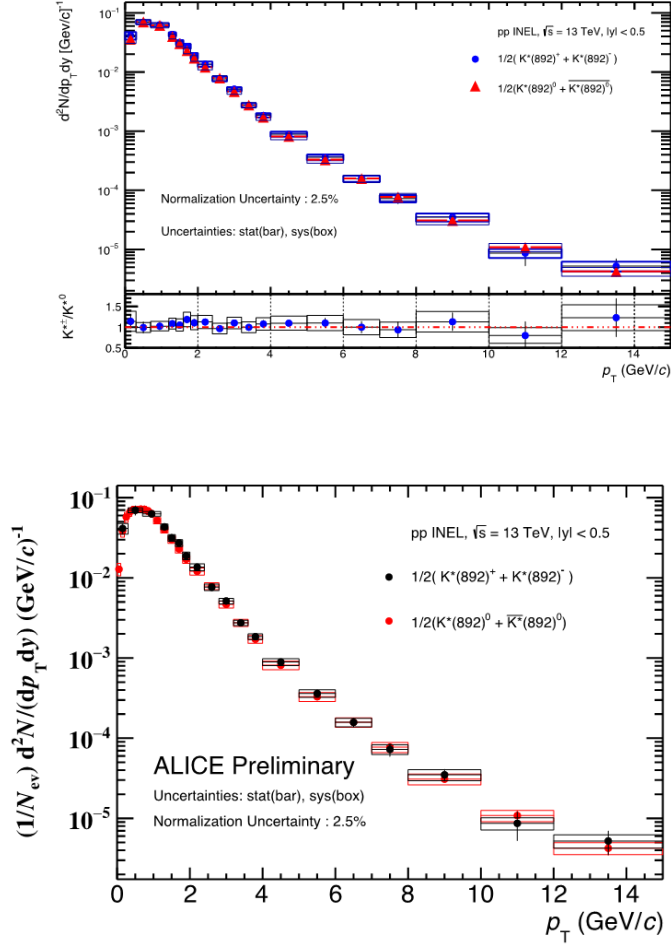


Fig. 29:  $K^*(892)^\pm$  corrected  $p_T$  spectrum (red stars) compared with the  $K^*(892)^0$  one (blue crosses) for pp collisions at  $\sqrt{s} = 13$  TeV. Only statistical errors are reported. Ratio of  $K^*(892)^0/K^*(892)^\pm$  in the bottom pad. Inelastic  $K^*(892)^\pm$  spectrum (black circles) is compared with the  $K^*(892)^0$  one (red circles) for pp collisions at  $\sqrt{s} = 13$  TeV. Statistical and systematic uncertainties are reported.

### 7.3 $dN/dy$ and mean $p_T$

The corrected spectrum was fitted with a Levy-Tsallis function, which describes both the exponential and power law shape of the spectrum at low and high transverse momentum, see Fig. 28.

$$\frac{d^2N}{dp_T dy} = p_T \frac{dN}{dy} \frac{(n-1)(n-2)}{nT[nT + m(n-2)]} \left(1 + \frac{\sqrt{m^2 - p_T^2} - m}{nT}\right)^{-n} \quad (14)$$

The  $p_T$ -integrated yield ( $dN/dy$ ) is obtained by integrating the spectrum in the measured range and extrapolating to zero  $p_T$  and to higher  $p_T$  by a Levy-Tsallis function. Then  $dN/dy$  is defined as  $\frac{dN}{dy} = I_{hist} + I_{extrapolated}$ , where  $I_{hist} = \int \Sigma 2\pi p_T f(p_T, y) dp_T$  in the measured range and  $I_{extrapolated} = \int 2\pi f(p_T, y) p_T dp_T$  in the extrapolated region.

Similarly, the mean transverse momentum ( $\langle p_T \rangle$ ) is defined as:

$\langle p_T \rangle = (\Sigma 2\pi p_T^2 f(p_T, y) dp_T + \int 2\pi f(p_T, y) p_T dp_T) / (I_{hist} + I_{extrapolated})$  where  $f(p_T, y)$  is the invariant yield.

**Table 1:**  $dN/dy$  and  $\langle p_T \rangle$  values and  $\chi^2/ndf$ ,  $n$  and  $T(\text{GeV})$  parameters of the Levy-Tsallis fit for  $K^*(892)^\pm$  and  $K^*(892)^0$  in pp collisions at  $\sqrt{s} = 13$  TeV.

| Particle       | $dN/dy$                       | $\langle p_T \rangle$ (GeV/c) | $\chi^2/ndf$ | $n$           | $T(\text{GeV})$   |
|----------------|-------------------------------|-------------------------------|--------------|---------------|-------------------|
| $K^*(892)^\pm$ | $0.110 \pm 0.005 \pm 0.01$    | $1.13 \pm 0.03 \pm 0.03$      | 0.309        | $7.4 \pm 0.4$ | $0.312 \pm 0.016$ |
| $K^*(892)^0$   | $0.104 \pm 0.0008 \pm 0.0108$ | $1.121 \pm 0.0005 \pm 0.032$  | 0.247        | $6.9 \pm 0.5$ | $0.300 \pm 0.016$ |

To calculate the integrated yield ( $dN/dy$ ) and the mean  $p_T$  ( $\langle p_T \rangle$ ) the macro

*ALICE/PHYSICS/PWGLF/SPECTRA/UTILS/YieldMean.C* was used. The measured spectrum is fitted with a Levy-Tsallis function in the fit range  $0 < p_T < 15$  GeV/c. Usually, the systematic uncertainties have two parts: one coming from systematic uncertainties of the spectrum and a second originated from the extrapolation of the spectrum to the unmeasured regions. However due the fact that the limit of the measured spectrum are (0,15) GeV/c the  $dN/dy$  and  $\langle p_T \rangle$  are estimated used only the measured points.

The values of  $dN/dy$  and  $\langle p_T \rangle$  and of the fit parameters are given in Tab. 1. The same values obtained for the  $K^*(892)^0$  analysis in the same collision system are also listed.

In Fig. 30 the  $K^*(892)^\pm/K$  ratio for pp collisions at  $\sqrt{s} = 13$  TeV is compared with the  $K^*(892)^0/K$  one for different systems and collision energies. The measured value for the  $K^{*\pm}$  is in agreement within the estimated errors with the  $K^*(892)^0$  one.

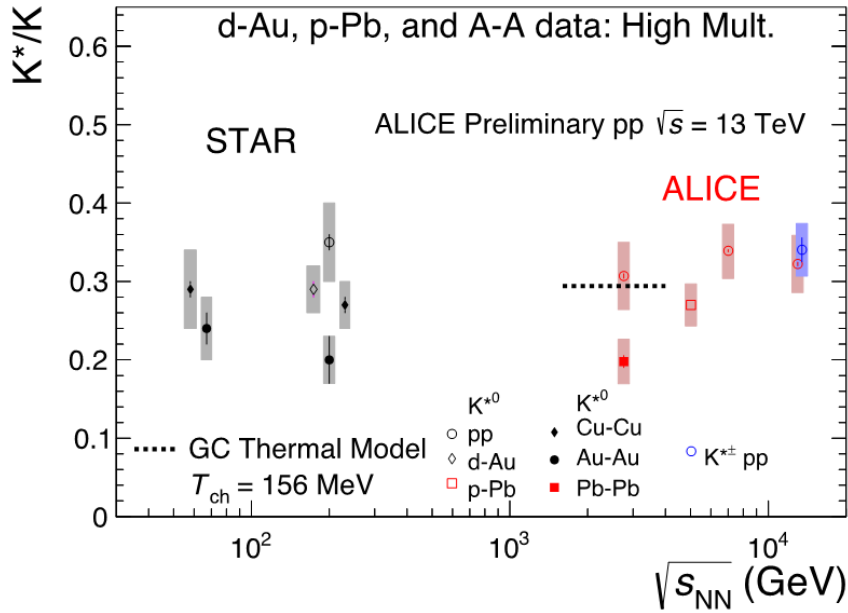


Fig. 30:  $K^*(892)^\pm/K$  ratio for pp collisions at  $\sqrt{s} = 13$  TeV compared with the  $K^*(892)^0/K$  one for different systems and collision energies. The symbol for  $K^*(892)^\pm$  at  $\sqrt{s} = 13$  TeV is slightly displaced to readability of the figure. The  $K^*(892)^0/K$  ratios were taken from ALI-PREL-106385.

## 7.4 Comparisons to models

In Fig. 31 the inelastic  $K^*(892)^\pm$  spectrum is compared with the PYTHIA 8 - Monash 2013, PYTHIA 6 - Perugia 2011, EPOS-LHC predictions. The LHC15g3a3 (PYTHIA8), LHC15g3c3 (PYTHIA6) and LHC16d3 (EPOS-LHC) production were used. The  $K^{*\pm}$  were generated without any trigger selection and with a check that the generated vertex is inside  $\pm 10$  cm.

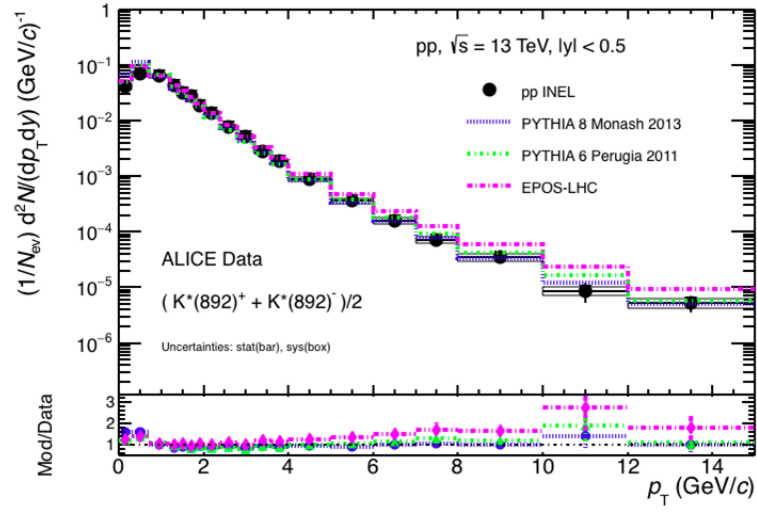


Fig. 31:  $K^*(892)^\pm$  inelastic  $p_T$  spectrum (red triangles) for pp collisions at  $\sqrt{s} = 13$  TeV compared with the  $p_T$  spectrum predicted by PYTHIA8- Monash 2013 (blue lines), PYTHIA 6 - Perugia 2011 (green lines), and EPOS-LHC (magenta lines).

## 8 Appendix

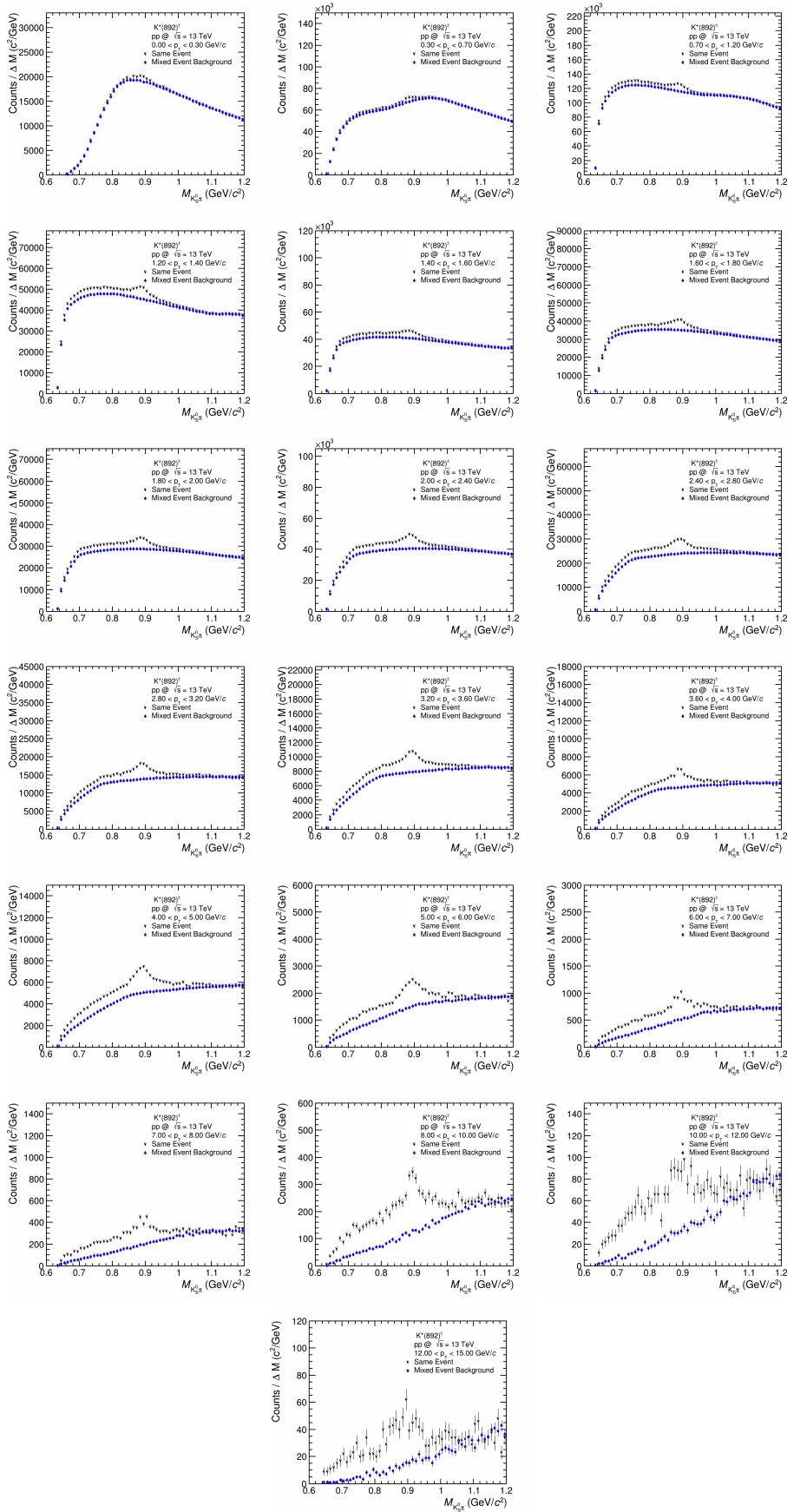


Fig. 32: The  $K_S^0 \pi^\pm$  invariant mass distribution in  $|y| < 0.5$  in pp collisions at 13 TeV for the different  $p_T$  bins. The background shape estimated using pairs from different events (event-mixing technique) is shown as empty green circles.

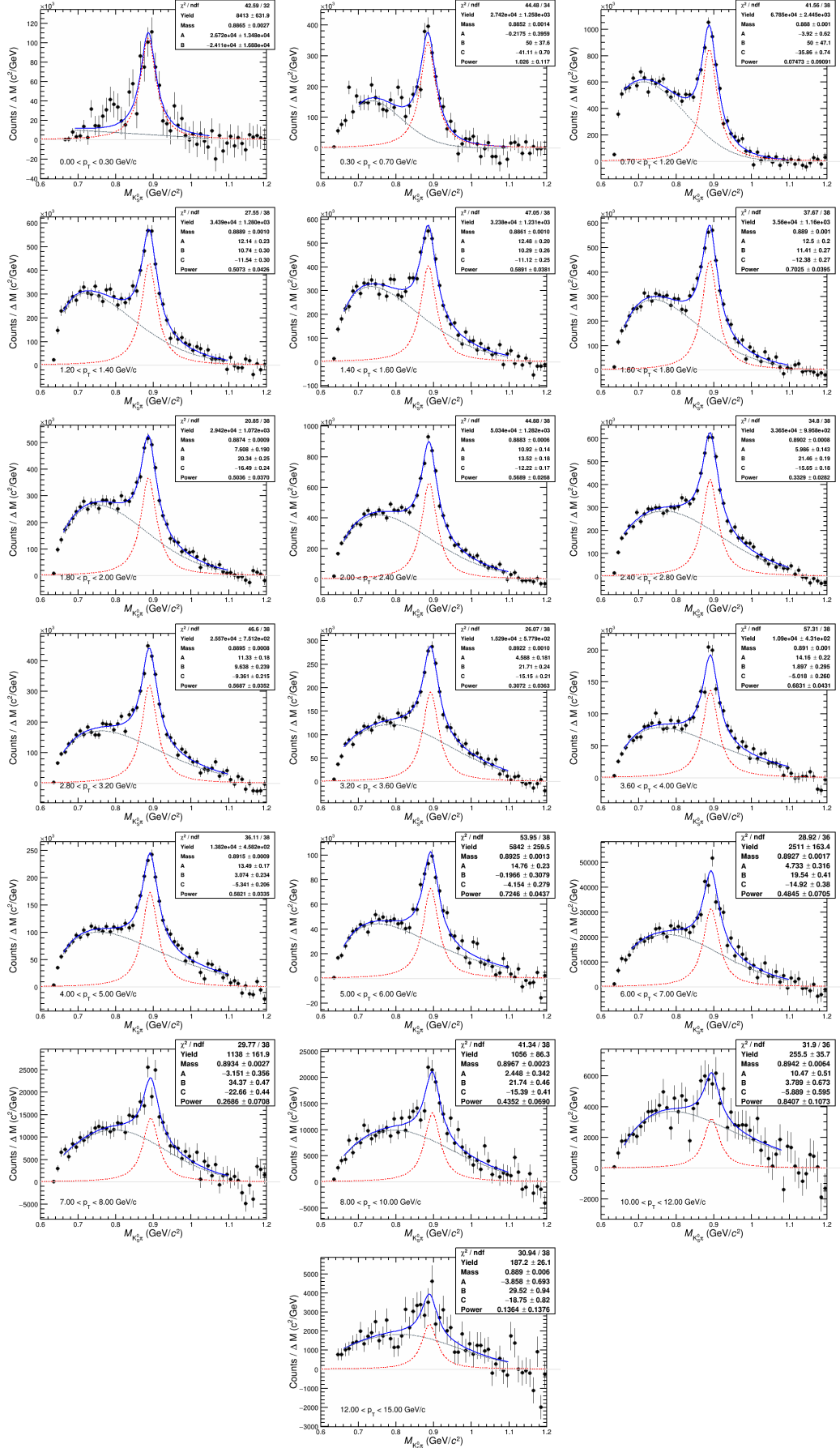


Fig. 33: The  $K_S^0 \pi^+$  invariant mass distribution in  $|y| < 0.5$  pp collisions at 13 TeV for the different  $p_T$  bins after background subtraction. The solid red curve is the results of the fit by eq. 4, the dashed blue (green) line describes the residual background (non-relativistic Breit-Wigner) distribution.

## References

- [1] S. Kundu and B. Mohanty Alice Analysis Note ANA-2975 " $K^*(892)^0$  resonance production in pp collisions at  $\sqrt{s} = 13$  TeV", <https://aliceinfo.cern.ch/Notes/node/469>
- [2] P. Kalinak, M. Sefcik, M. Bombara, I. Kralik, Alice Analysis Note ANA-2586 " $K_S^0$ ,  $\Lambda$  and  $\bar{\Lambda}$  production in proton - proton collisions at  $\sqrt{s} = 13$  TeV", <https://aliceinfo.cern.ch/Notes/node/425>
- [3] C. Patrignani *et al.*, Chin. Phys. C40 (2016) 100001
- [4] J. Adams *et al.* (STAR collaboration) " $\rho$  production and possible modification in Au+Au and p+p collisions at  $\sqrt{s_{NN}} = 200$  GeV", Phys. Rev. Lett., 92 (2004) 092301.
- [5] V. Riabov, " $\rho \rightarrow \pi\pi$  production in pp collisions at  $\sqrt{s} = 2.76$  TeV with TPC-PID", ALICE-ANA-2179, <https://aliceinfo.cern.ch/Notes/node/374>
- [6] T. Ullrich and Z. Xu, "Treatment of errors in efficiency calculations" (Preprint physics/ 0701199v1) (2007)
- [7] R. Barlow, "Systematic errors: facts and fictions" (Preprint hep-ex/0207026v1) (2002)
- [8] A. Andronic *et al.* (ALICE Collaboration) 2015 ALICE-ANA-2015-2564 URL <https://aliceinfo.cern.ch/Notes/node/415>
- [9] J. Adam *et al.* (ALICE Coll.), "Production of  $K^*(892)^0$  and  $\phi(1020)$  in p-Pb collisions at  $\sqrt{s_{NN}} = 5.02$  TeV", Eur. Phys. J. C 76 (2016) 245.
- [10] A. Knospe, "Measurement of  $\phi(1020)$  mesons at mid-rapidity in minimum-bias pp collisions at  $\sqrt{s} = 13$  TeV", ALICE-ANA-2016-2955 June 16, 2016